Ultra-violet imaging of the night-time earth by EUSO-Balloon towards space-based ultra-high energy cosmic ray observations

(Article begins on next page)

31 December 2024

Ultra-violet imaging of the night-time earth by EUSO-Balloon towards space-based ultra-high energy cosmic ray observations.

G. Abdellaoui[h], S. Abe[aw], J.H. Adams Jr.[cf], A. Ahriche[e], D. Allard[l],
L. Allen[cd], G. Alonso[bw], L. Anchordoqui[ch], A. Anzalone[y,u], Y. Arai[ay],
K. Asano[ak], R. Attallah[c], H. Attoui[a], M. Ave Pernas[bv], S. Bacholle[ce],
M. Bakiri[a], P. Baragatti[ae], P. Barrillon[j], S. Bartocci[ae], J. Bayer[q],
B. Beldjilali[h], T. Belenguer[bu], N. Belkhalfa[a], R. Bellotti[r,s], A. Belov[bp],
K. Belov[cg], K. Benmessai[a], M. Bertaina[ab,ac], P.L. Biermann[o],
S. Biktemerova[bn], F. Bisconti[ab], N. Blanc[bz], J. Błęcki[bl], S. Blin-Bondil[k],
P. Bobik[br], M. Bogomilov[i], E. Bozzo[ca], S. Briz[cd], A. Bruno[s], K.S. Caballero[bh],
F. Cafagna[r], D. Campana[w], J-N. Capdevielle[l], F. Capel[by], A. Caramete[bm],
L. Caramete[bm], P. Carlson[by], R. Caruso[t,u], M. Casolino[az,z], C. Cassardo[ab,ac],
A. Castellina[ab,ad], C. Catalano[l], O. Catalano[y,u], A. Cellino[ab,ad], M. Chikawa[ai],
G. Chiritoi[bm], M.J. Christl[ci], V. Connaughton[cf], L. Conti[ae], G. Cordero[bd],
G. Cotto[ab,ac], H.J. Crawford[cc], R. Cremonini[ac], S. Csorna[cj], A. Cummings[ce],
S. Dagoret-Campagne[j], A.J. de Castro[cd], C. De Donato[z], C. de la Taille[k],
C. De Santis[z], L. del Peral[bv], M. Di Martino[ad], A. Diaz Damian[m], T. Djemil[c],
I. Dutan[bm], A. Ebersoldt[o], T. Ebisuzaki[az], R. Engel[o], J. Eser[ce], F. Fenu[ab,ac],
S. Fernández-González[bt], S. Ferrarese[ab,ac], M. Flamini[ae], C. Fornaro[ae],
M. Fouka[b], A. Franceschi[v], S. Franchini[bw], C. Fuglesang[by], T. Fujii[ak],
J. Fujimoto[ay], M. Fukushima[ak], P. Galeotti[ab,ac], E. García-Ortega[bt],
G. Garipov[bp], E. Gascón[bt], J. Genci[bs], G. Giraudo[ab], C. González Alvarado[bu],
P. Gorodetzky[l], R. Greg[ce], F. Guarino[w,x], A. Guzmán[q], Y. Hachisu[az],
M. Haiduc[bm], B. Harlov[bo], A. Haungs[o], J. Hernández Carretero[bv],
W. Hidber Cruz[bd], D. Ikeda[ak], N. Inoue[at], S. Inoue[az], F. Isgrò[w,af], Y. Itow[aq],
T. Jammer[p], S. Jeong[bc], E. Joven[bx], E.G. Judd[cc], A. Jung[l], J. Jochum[p],
F. Kajino[al], T. Kajino[ao], S. Kalli[f], I. Kaneko[az], Y. Karadzhov[i],
J. Karczmarczyk[bk,2], K. Katahira[az], K. Kawai[az], Y. Kawasaki[az,2],
A. Kedadra[a], H. Khales[a], B.A. Khrenov[bp], Jeong-Sook Kim[ba],
Soon-Wook Kim[ba], M. Kleifges[o], P.A. Klimov[bp], D. Kolev[i], H. Krantz[ce],
I. Kreykenbohm[n], J.F. Krizmanic[ci], K. Kudela[br], Y. Kurihara[ay],
A. Kusenko[ax], E. Kuznetsov[cf], A. La Barbera[y,u], A. Lachaud[l], H. Lahmar[a],
F. Lakhdari[g], O. Larsson[by], J. Lee[bc], J. Licandro[bx], L. López Campano[bt],
F. López[cd], M.C. Maccarone[y,u], S. Mackovjak[br,1], M. Mahdi[a], D. Maravilla[bd],
L. Marcelli[z], J.L. Marcos[bt], A. Marini[v], W. Marszał[bk], K. Martens[ax],
Y. Martín[bx], O. Martinez[bf], M. Martucci[v], G. Masciantonio[z], K. Mase[ag],

M. Mastafa[cf], R. Matev[i], J.N. Matthews[ck], N. Mebarki[d], G. Medina-Tanco[bd],

M.A. Mendoza[bg], A. Menshikov[o], A. Merino[bt], J. Meseguer[bw], S.S. Meyer[cd],

J. Mimouni[d], H. Miyamoto[ab,ac], Y. Mizumoto[ao], A. Monaco[r,s],

J.A. Morales de los Ríos[bv], C. Moretto[m], S. Nagataki[az], S. Naitamor[b],

T. Napolitano[v], R. Nava[bd], A. Neronov[ca], K. Nomoto[ax], T. Nonaka[ak],

T. Ogawa[az], S. Ogio[ar], H. Ohmori[az], A.V. Olinto[cd], P. Orleański[bl],

G. Osteria[w], A. Pagliaro[y,u], W. Painter[o], M.I. Panasyuk[bp], B. Panico[w],

E. Parizot[l], I.H. Park[bc], B. Pastircak[br], T. Patzak[l], T. Paul[ch],

I. Pérez-Grande[bw], F. Perfetto[w,x], T. Peter[cb], P. Picozza[z,aa,az], S. Pindado[bw],

L.W. Piotrowski[az], S. Piraino[q], L. Placidi[ae], Z. Plebaniak[bk], S. Pliego[bd],

A. Pollini[bz], Z. Polonsky[ce], E.M. Popescu[bm], P. Prat[l], G. Prévôt[l], H. Prieto[bv],

G. Puehlhofer[q], M. Putis[br], J. Rabanal[j], A.A. Radu[bm], M. Reyes[bx],

M. Rezazadeh[cd], M. Ricci[v], M.D. Rodríguez Frías[bv], F. Ronga[v], G. Roudil[m],

I. Rusinov[i], M. Rybczyński[bj], M.D. Sabau[bu], G. Sáez Cano[bv], H. Sagawa[ak],

Z. Sahnoune[b], A. Saito[am], N. Sakaki[ak], H. Salazar[bf], J.C. Sanchez Balanzar[bd],

J.L. Sánchez[bt], A. Santangelo[q], A. Sanz-Andrés[bw], M. Sanz Palomino[bu],

O. Saprykin[bq], F. Sarazin[ce], M. Sato[au], T. Schanz[q], H. Schieler[o], V. Scotti[w,x],

S. Selmane[l], D. Semikoz[l], M. Serra[bx], S. Sharakin[bp], H.M. Shimizu[ap],

K. Shinozaki[ab,ac,1], T. Shirahama[at], B. Spataro[v], I. Stan[bm], T. Sugiyama[ap],

D. Supanitsky[bd], M. Suzuki[as], B. Szabelska[bk], J. Szabelski[bk], N. Tajima[az],

T. Tajima[az], Y. Takahashi[au], H. Takami[ay], M. Takeda[ak], Y. Takizawa[az],

M.C. Talai[c], C. Tenzer[q], S.B. Thomas[ck], O. Tibolla[bi], L. Tkachev[bn],

H. Tokuno[av], T. Tomida[an], N. Tone[az], S. Toscano[ca], M. Traïche[a], R. Tsenov[i],

Y. Tsunesada[ar], K. Tsuno[az], J. Tubbs[cf], S. Turriziani[az], Y. Uchihori[ah],

O. Vaduvescu[bx], J.F. Valdés-Galicia[bd], P. Vallania[ab,ad], G. Vankova[i],

C. Vigorito[ab,ac], L. Villaseñor[be], B. Vlcek[bv], P. von Ballmoos[m], M. Vrabel[bs],

S. Wada[az], J. Watanabe[ao], J. Watts Jr.[cf], M. Weber[o], R. Weigand Muñoz[bt],

A. Weindl[o], L. Wiencke[ce], M. Wille[n], J. Wilms[n], Z. Włodarczyk[bj],

T. Yamamoto[al], J. Yang[bb], H. Yano[as], I.V. Yashin[bp], D. Yonetoku[aj],

S. Yoshida[ag], R. Young[ci], I.S. Zgura[bm], M.Yu. Zotov[bp], A. Zuccaro Marchi[az]

[a]*Centre for Development of Advanced Technologies (CDTA), Algiers, Algeria*
[b]*Department of Astronomy, Center of Research in Astronomy, Astrophysics, and Geophysics (CRAAG), Algiers, Algeria*
[c]*LPR at Department of Physics, Faculty of Sciences, University Badji Mokhtar, Annaba, Algeria*
[d]*Laboratory of Mathematics and Sub-Atomic Physics (LPMPS), University Constantine I, Constantine, Algeria*
[e]*Laboratory of Theoretical Physics LPT, University of Jijel, Jijel, Algeria*
[f]*Department of Physics, Faculty of Sciences, University of M'sila, M'sila, Algeria*
[g]*Research Unit on Optics and Photonics, UROP-CDTA, Sétif, Algeria*
[h]*Telecom Laboratory, Faculty of Technology, University Abou Bekr Belkaid, Tlemcen, Algeria*
[i]*St. Kliment Ohridski University of Sofia, Bulgaria*
[j]*LAL, Université Paris-Sud, CNRS/IN2P3, Orsay, France*
[k]*Omega, Ecole Polytechnique, CNRS/IN2P3, Palaiseau, France*
[l]*APC, Université Paris Diderot, CNRS/IN2P3, CEA/Irfu, Observatoire de Paris, Sorbonne Paris Cité, Paris, France*
[m]*IRAP, Université de Toulouse, CNRS, Toulouse, France*
[n]*ECAP, University of Erlangen-Nuremberg, Erlangen, Germany*

2

[o]Karlsruhe Institute of Technology (KIT), Karlsruhe, Germany

[p]Experimental Physics Institute, Kepler Center, University of Tübingen, Tübingen, Germany

[q]Institute for Astronomy and Astrophysics, Kepler Center, University of Tübingen, Tübingen, Germany

[r]Istituto Nazionale di Fisica Nucleare – Sezione di Bari, Bari, Italy

[s]Università degli Studi di Bari Aldo Moro, Bari, Italy

[t]Dipartimento di Fisica e Astronomia – Università di Catania, Catania, Italy

[u]Istituto Nazionale di Fisica Nucleare – Sezione di Catania, Catania, Italy

[v]Istituto Nazionale di Fisica Nucleare – Laboratori Nazionali di Frascati, Frascati, Italy

[w]Istituto Nazionale di Fisica Nucleare – Sezione di Napoli, Naples, Italy

[x]Dipartimento di Scienze Fisiche, Università di Napoli Federico II, Naples, Italy

[y]INAF – Istituto di Astrofisica Spaziale e Fisica Cosmica di Palermo, Palermo, Italy

[z]Istituto Nazionale di Fisica Nucleare – Sezione di Roma Tor Vergata, Rome, Italy

[aa]Dipartimento di Fisica, Università di Roma Tor Vergata, Rome, Italy

[ab]Istituto Nazionale di Fisica Nucleare – Sezione di Torino, Turin, Italy

[ac]Dipartimento di Fisica, Università di Torino, Turin, Italy

[ad]Osservatorio Astrofisico di Torino, Istituto Nazionale di Astrofisica, Pino Torinese, Italy

[ae]Uninettuno University, Rome, Italy

[af]DIETI, Università degli Studi di Napoli Federico II, Naples, Italy

[ag]Chiba University, Chiba, Japan

[ah]National Institute of Radiological Sciences, Chiba, Japan

[ai]Kindai University, Higashi-Osaka, Japan

[aj]Kanazawa University, Kanazawa, Japan

[ak]Institute for Cosmic Ray Research, University of Tokyo, Kashiwa, Japan

[al]Konan University, Kobe, Japan

[am]Kyoto University, Kyoto, Japan

[an]Shinshu University, Nagano, Japan

[ao]National Astronomical Observatory, Mitaka, Japan

[ap]Nagoya University, Nagoya, Japan

[aq]Institute for Space-Earth Environmental Research, Nagoya University, Nagoya, Japan

[ar]Graduate School of Science, Osaka City University, Japan

[as]Institute of Space and Astronautical Science/JAXA, Sagamihara, Japan

[at]Saitama University, Saitama, Japan

[au]Hokkaido University, Sapporo, Japan

[av]Interactive Research Center of Science, Tokyo Institute of Technology, Tokyo, Japan

[aw]Nihon University Chiyoda, Tokyo, Japan

[ax]University of Tokyo, Tokyo, Japan

[ay]High Energy Accelerator Research Organization (KEK), Tsukuba, Japan

[az]RIKEN, Wako, Japan

[ba]Korea Astronomy and Space Science Institute (KASI), Daejeon, Republic of Korea

[bb]Ewha Womans University, Seoul, Republic of Korea

[bc]Sungkyunkwan University, Seoul, Republic of Korea

[bd]Universidad Nacional Autónoma de México (UNAM), Mexico City, Mexico

[be]Universidad Michoacana de San Nicolas de Hidalgo (UMSNH), Morelia, Mexico

[bf]Benemérita Universidad Autónoma de Puebla (BUAP), Puebla, Mexico

[bg]Centro de Desarrollo Aeroespacial – Instituto Politécnico National (CDA-IPN), Mexico City, Mexico

[bh]Universidad Autónoma de Chiapas (UNACH), Chiapas, Mexico

[bi]Centro Mesoamericano de Física Teórica (MCTP), Chiapas, Mexico

[bj]Jan Kochanowski University, Institute of Physics, Kielce, Poland

[bk]National Centre for Nuclear Research, Lodz, Poland

[bl]Space Research Centre of the Polish Academy of Sciences (CBK), Warsaw, Poland

[bm]Institute of Space Science ISS, Magurele, Romania

[bn]Joint Institute for Nuclear Research, Dubna, Russia

[bo]Central Research Institute of Machine Building, TsNIIMash, Korolev, Russia

3

143   [bp]*Skobeltsyn Institute of Nuclear Physics, Lomonosov Moscow State University, Moscow,*

144   *Russia*

145   [bq]*Space Regatta Consortium, Korolev, Russia*

146   [br]*Institute of Experimental Physics, Kosice, Slovakia*

147   [bs]*Technical University Kosice (TUKE), Kosice, Slovakia*

148   [bt]*Universidad de León (ULE), León, Spain*

149   [bu]*Instituto Nacional de Técnica Aeroespacial (INTA), Madrid, Spain*

150   [bv]*Universidad de Alcalá (UAH), Madrid, Spain*

151   [bw]*Universidad Politécnica de Madrid (UPM), Madrid, Spain*

152   [bx]*Instituto de Astrofísica de Canarias (IAC), Tenerife, Spain*

153   [by]*KTH Royal Institute of Technology, Stockholm, Sweden*

154   [bz]*Swiss Center for Electronics and Microtechnology (CSEM), Neuchâtel, Switzerland*

155   [ca]*ISDC Data Centre for Astrophysics, Versoix, Switzerland*

156   [cb]*Institute for Atmospheric and Climate Science, ETH Zürich, Zurich, Switzerland*

157   [cc]*Space Science Laboratory, University of California, Berkeley, USA*

158   [cd]*University of Chicago, Chicago, USA*

159   [ce]*Colorado School of Mines, Golden, USA*

160   [cf]*University of Alabama in Huntsville, Huntsville, USA*

161   [cg]*NASA Jet Propulsion Laboratory, Pasadena, USA*

162   [ch]*Lehman College, City University of New York (CUNY), New York, USA*

163   [ci]*NASA – Marshall Space Flight Center, Huntsville, USA*

164   [cj]*Vanderbilt University, Nashville, USA*

165   [ck]*University of Utah, Salt Lake City, USA*

166 **Abstract**

The JEM-EUSO (Joint Experiment Missions for the Extreme Universe Space Observatory) program aims at developing Ultra-Violet (UV) fluorescence telescopes for efficient detections of Extensive Air Showers (EASs) induced by Ultra-High Energy Cosmic Rays (UHECRs) from satellite orbit. In order to demonstrate key technologies for JEM-EUSO, we constructed the EUSO-Balloon instrument that consists of a $\sim$1 m^2 refractive telescope with two Fresnel lenses and an array of multi-anode photo-multiplier tubes at the focus. Distinguishing it from the former balloon-borne experiments, EUSO-Balloon has the capabilities of single photon counting with a gate time of 2.3 µs and of imaging with a total of 2304 pixels. As a pathfinder mission, the instrument was launched for an 8 hour stratospheric flight on a moonless night in August 2014 over Timmins, Canada. In this work, we analyze the count rates over $\sim$2.5 hour intervals. The measurements are of diffuse light, e.g. of airglow emission, back-scattered from the Earth's atmosphere as well as artificial light

4

sources. Count rates from such diffuse light are a background for EAS detections in future missions and relevant factor for the analysis of EAS events. We also obtain the geographical distribution of the count rates over a $\sim$780 km^2 area along the balloon trajectory. In developed areas, light sources such as the airport, mines, and factories are clearly identified. This demonstrates the correct location of signals that will be required for the EAS analysis in future missions. Although a precise determination of count rates is relevant for the existing instruments, the absolute intensity of diffuse light is deduced for the limited conditions by assuming spectra models and considering simulations of the instrument response. Based on the study of diffuse light by EUSO-Balloon, we also discuss the implications for coming pathfinders and future space-based UHECR observation missions.

1. Introduction

Ultra-High Energy Cosmic Rays (UHECRs) with energies, E_0, of several times greater than 10^{19} eV are extremely rare events and their origin is not yet known [1]. To resolve this long-standing problem, it is essential to observe large numbers of UHECRs for the systematic study of their arrival direction distribution on the celestial sphere. Recent reports by the Pierre Auger Observatory (Auger) [2] and the Telescope Array (TA) [3] agree that, despite a possible discrepancy in the energy scales, the observed energy spectra show suppression of the fluxes of UHECRs above $\sim$5 $\times$ 10^{19} eV in comparison to an extrapolation from lower energies [4]. Above this energy, UHECRs have been observed with the fluxes of the order of a few events per square kilometer per century or even millennium.

Since the early 21st Century, large-scale ground-based UHECR observations have been led by Auger [5] and TA [6] using particle detector arrays that cover

an observation area, S_{obs}, of $\sim$3000 km^2 and $\sim$700 km^2, respectively. Cosmic rays are observed by detecting secondary particles in the induced Extensive Air Showers (EASs) [1]. These experiments have their exposures to UHECRs in different parts of the celestial sphere according to their geographic positions. Recently excesses of UHECRs are reported as the middle-scale anisotropy in the arrival direction distribution above $\sim 8 \times 10^{18}$ eV by Auger [7] and above $\sim 5 \times 10^{19}$ eV by TA [8, 9], respectively. At the even higher energies, still larger exposures are required to study it in more detail.

Both experiments also operate a few stations of multiple 'fluorescence telescopes' each of which has a $\sim$10 m^2 reflector and an array of Photo-Multiplier Tubes (PMTs) at the focus [10, 11]. Cosmic rays are observed by the 'fluorescence technique', imaging the Ultra-Violet (UV) fluorescence light emitted from the nitrogen molecules excited by the charged particles in the EAS [1]. This light has a characteristic line spectrum in the $\sim$290 – 430 nm band [12]. EAS events are seen as a bright point-like spot moving at the speed of light above the 'background' light. Such light originates from both natural, i.e., terrestrial and astronomical, and artificial light sources and increases the noise level on the instrument.

Since the 1980s, space-based UHECR observations by means of the fluorescence technique have been conceptually investigated and several missions have been proposed [13, 14, 15, 16]. A single telescope with a few tens of degrees wide Field-of-View (FoV) from a satellite orbit allows utilizing the night-time atmosphere as a vast particle calorimeter to efficiently increase the exposure over the whole celestial sphere. The EAS signals are only detectable when significantly above the noise level. The energy and arrival direction of the incident UHECRs are determined by analyzing the spatial and temporal development of such signals above this level [17, 18, 19]. In this way, it is important to understand the noise level when estimating the detection capabilities of the instruments and the quality of data analysis.

In 2016, the TUS instrument was launched to start space-based UHECR observations in an orbit at $\sim$500 km above sea level (asl.) [20]. Using a $\sim$2 m^2

6

reflective Fresnel telescope with 256 PMTs, it covers a $\sim 9°$ FoV corresponding to an order of $S_{\mathrm{obs}} \sim 6000$ km^2 area. Simulation studies show that this instrument is capable of detecting EASs from UHECRs with 10^{20} eV energies.

The JEM-EUSO (Joint Experiment Missions for the Extreme Universe Space Observatory) program [21] is one of the mainstream projects. As the baseline, an ultra-wide FoV telescope was proposed using ~ 4.5 m^2 refractive optics with three double-sided Fresnel lenses, aiming at UHECR observations over an $S_{\mathrm{obs}} \sim 10^5$ km^2 area from the International Space Station (ISS) at ~ 400 km asl. [22]. This optical system was designed to achieve a wide enough FoV with high enough Signal-to-Noise Ratio (SNR) on the photo-detector, this being a requirement in the development of such detectors. To test the key technologies for JEM-EUSO, we conducted and planned pathfinders on the ground, on balloons and the ISS. Including the experience from TUS, the outcomes from these pathfinders can be also applied to future missions such as KLYPVE-EUSO [23, 24] and POEMMA [25].

In August 2014, a stratospheric flight of EUSO-Balloon was carried out from Timmins (ON), Canada. It reached a float altitude at ~ 38 km asl. The EUSO-Balloon mission allowed for a full end-to-end test of a JEM-EUSO prototype consisting of the key subsystems for a space experiment. The instrument performed UV imaging of the night-time earth that allows for a better understanding and scientific interpretation of future space-based UHECR observations.

For efficient detections of EASs, given constraints on the data downlink capacity of the mission, the noise level on the photo-detectors should be carefully monitored. It affects not only the trigger algorithms for real-time EAS detection in orbit, but also introduces errors in offline, ground-based data analysis. In this work, we present the results and discussions on such noise from UV light seen by EUSO-Balloon from both natural and artificial sources. Hereafter, we define 'background' light as the sum of any light in the $\sim 300 - 500$ nm wavelength band from the atmosphere or the earth below, as seen by the nadir-pointing instrument.

This paper is organized as follows: Section 2 summarizes the existing knowledge of UV light from the night-time earth and atmosphere and the measurements obtained by the former balloon experiments. Section 3 describes the specifications of the EUSO-Balloon mission and the data used in this work. Section 4 presents the methods of the analysis. Section 5 shows the main results. Section 6 gives interpretations of the results, implications for space-based UHECR observations and the outlook for future missions. Section 7 concludes this work.

2. UV light from the night-time earth

2.1. UV light as a background for UHECR observations

In terms of the effect on UHECR observations, the background consists of light components from both persistent and local sources in the UV band; the former is due to diffuse light sources illuminating the whole FoV, thus reducing the observation time and the latter appears transiently, reducing a part of the instantaneous observation area. The local component is often so intense that the trigger algorithms for detecting EAS events are hampered. In terms of studying the background light relevant for the detections of EASs, only diffuse light plays a role and this component should be quantified for the impact on the noise due to its intensity.

The distribution of the local light sources such as cities can be predicted in advance along the orbit of a space-based observatory. Influence from the isolated light sources only occurs where such sources pass through the FoV. The trigger algorithms can be designed to remain operational in the rest of the FoV [26, 27]. At higher geomagnetic latitudes, the entire FoV may occasionally be filled by the aurora. This can be monitored by the telescope itself and recognized by using external information about the geomagnetic storm [28]. Sudden events such as lightning and transient luminous events persist for durations of the order of milliseconds. This is far slower than the tens-to-hundreds-microsecond-scale of EASs, thus the affected area and time can be recognized. On these occasions,

8

it is only important to quantify the affected fraction of the instantaneous observation area rather than the light intensity.

On moonless, dark nights, the airglow is the dominant source in the $\sim 300-400$ nm band. It is emitted when the disassociated oxygen atoms recombine to molecules at around $80-100$ km asl. near the mesopause. The emission mechanisms are well understood. They produce a mixture of the Herzberg I, Herzberg II and Chamberlain emissions [29]. The intensity of the airglow emission, as well as by the position over the Earth, changes on various time scales, i.e., seasonally, daily or even more frequently [30, 31, 32]. In orbit, the airglow light is measured as a sum of the direct light from the emission altitude and back-scattered light from the atmosphere, clouds, and the Earth's surface.

By pointing the instrument downwards, extraterrestrial light such as starlight and zodiacal light originating above the flight level only contributes to the noise as back-scattered light. Such situations are realized when the Moon is near the New Moon phase or lies near the horizon. The properties of such light have been discussed in Refs. [22, 33] and references therein.

2.2. Former balloon-borne measurements

As part of the drive for space-based UHECR observations, there have been several balloon-borne experiments aiming at investigating background light [34, 35, 36, 37]. A major goal of these experiments was to determine the absolute intensity, I_0, of the diffuse light under clear atmosphere conditions in moonless night. Results have been presented by two groups.

The Background Bypass (BaBy) balloon experiment [34] was first carried out over the land and sea off Sicily, Italy, at ~ 26 km asl. on July 30, 1998. The instrument was purely designed for diffuse light measurements that consisted of two sets of collimators and PMTs mounted with UV band-pass filters. The estimated I_0 value over the sea without ambient light of the populated areas was $\sim 400-450$ photons m^{-2} sr^{-1} ns^{-1} in the $300-500$ nm band. The other flight of BaBy reaching ~ 39 km asl. took place over the Mediterranean Sea on

July 11, 2002 [35]. The average I_0 value was 310 photons m^{-2} sr^{-1} ns^{-1} in the $300-400$ nm band. Another flight attempt in 2001 was reported with more than twice the intensity in comparison with the above value. We consider that it was due to the low flight altitude of $\sim15-30$ km and possible light pollution by the artificial light.

The NIGHTGLOW balloon experiment took place over Texas, USA, at ~30 km asl. on July 5, 2000 [36]. The instrument was composed of elements used for real fluorescence telescopes; a ~36 cm diameter spare mirror and UV band-pass filters from the High Resolution Fly's Eye (HiRes) experiment [38] and two PMTs from the Fly's Eye experiment [39]. These filters were selected for the maximum SNR for EAS detections. The I_0 value in the nadir direction was found to be 300 ± 41 photons m^{-2} sr^{-1} ns^{-1} in the $300-400$ nm band. By pointing the instrument to the zenith, the total intensity of the downward component was estimated to be 691 ± 34 photons m^{-2} sr^{-1} ns^{-1}.

The latest discussions on the I_0 values were given in this Journal by NIGHTGLOW and by the Tatiana satellite [40]. Even under similar conditions, it is difficult to compare different measurements due to the variability of airglow emissions and responses of the instruments. These values have been used as references for simulations to estimate the expected noise level on the instrument when designing fluorescence telescopes.

3. EUSO-Balloon

EUSO-Balloon was a pathfinder mission for the JEM-EUSO program led by the French space agency CNES (*Centre National d'Études Spatiales*) in coordination with the JEM-EUSO collaboration. A full description of the mission and scientific payload is specified in Ref. [41].

3.1. The EUSO-Balloon telescope

The EUSO-Balloon telescope is the main instrument of the balloon payload with a total mass of 467 kg. It is installed with crash rings, designed to protect

10

333 the instrument in the case of landing on dry land as well as a floater to keep
334 the electronics subsystems dry in the case of a possible water landing [42, 43].

335 EUSO-Balloon is capable of imaging in the UV band. This is a
336 major difference when compared to the former experiments. The telescope
337 consists of two Fresnel lenses made of 8 mm thick PMMA, UV transmitting
338 polymethylmethacrylate [44, 45]. Based on the technologies developed for
339 JEM-EUSO [46], the lenses were fabricated as 1.2 m diameter circular lenses
340 and then were cut to form a square of side 1 m with round corners. The nominal
341 entrance aperture, S_{opt}, is 0.96 m^2. To avoid any damage during landing, the
342 optics is recessed inside the overhanging walls. These walls are extended beyond
343 the front lens to act as a baffle, blocking photons from large off-axis angles.

344 A Photo-Detector Module (PDM) [47] is placed at the focus of the optics.
345 It is formed of 36 (= 6 × 6) Multi-Anode PMTs (MAPMTs; Hamamatsu
346 R11890-M64) [48, 49]. They are aligned with a 27.5 mm pitch. Nine squares of
347 four (= 2 × 2) MAPMTs are both mechanically and operationally grouped to
348 the units called Elementary Cells (ECs). Excluding the central unit, the ECs
349 are slightly inclined up to 2.48° to approximately follow the aspherical geometric
350 focal surface of the optics.

351 Every MAPMT has 64 channels in an array of 8 × 8 pixels. With each pixel
352 being a square of 2.88 mm on a side, the photocathode of an MAPMT effectively
353 covers a square area of side ∼23 mm (= 8 × 2.88 mm). A 2 mm thick band-pass
354 filter, Schott BG3 [50], is mounted on each MAPMT. The filters have a surface
355 dimension of a 27 mm square, allowing the collection of some photons falling on
356 the dead spaces between MAPMTs.

357 The sensitivity of the instrument is determined by the detection efficiency
358 of the MAPMTs, the transmittance of the BG3 filters and the response of the
359 optical system. The overall efficiency is highest in the ∼330 – 400 nm band
360 where dominant lines of fluorescence light lie to give a more precise energy
361 estimation of the incident UHECRs. The sensitive range extends between ∼250
362 and ∼500 nm. The lower limit is due to the transmittance of PMMA lenses,
363 while the upper limit is given by that of BG3 filters and the quantum efficiency

11

of the MAPMTs. It is worth mentioning that the sensitivity above $\sim$400 nm allows the collection of more of the Cherenkov light produced in the EASs. This light is in general not desirable for ground-based fluorescence telescopes since it introduces uncertainties in the analysis of detected EAS events [51]. Seen from above, such light is back-scattered from the Earth's surface or clouds and allows for a more precise determination of the arrival direction of UHECRs by constraining the geometry of EAS events [17, 52].

For the control of electronics subsystems, the Data Processor (DP) system [53] is employed. It controls front-end electronics, provides signals for time synchronization and triggers, handles the interfaces to tele-commands and to the telemetry system, and operates many other tasks. On a total of 2304 ($= 36 \times 64$) channels, single photon counting was performed. Data used in this work were acquired by two different trigger modes using the CPU command at $\sim$19 Hz or the GPS synchronous signals at 20 Hz. Following a trigger, 128 samples, or one 'packet', of counts, n, were acquired on all pixels every 2.5 μs. The readout duration, $\tau_{\mathrm{GTU}} = 2.3$ μs, of each sample is called the Gate Time Unit (GTU), hereafter [54, 55].

This duration was originally chosen to be 2.5 μs. This is the time that it takes light to travel through the atmosphere across one pixel as imaged by the original JEM-EUSO design from the ISS [56]. The choice of 128 samples was made for buffering the data of EAS events seen in a PDM of JEM-EUSO as well as a sufficient time before and after the event. These parameters have been unchanged in the updated designs. The EUSO-Balloon instrument represents one detection module of the proposed future space instruments which may have more than 50 PDMs [24]. Thus it uses a similar time scale and sampling in the data acquisition despite the much faster apparent speed of light crossing the FoV.

In this work, we define a reference Cartesian coordinate system for the analysis of the acquired data. Seen from the optical axis through the lenses, we take the reference x- and y- axes, to be parallel to the sides of the PDM and the lenses, projected on the photocathode plane of the central EC unit.

12

3.2. The EUSO-Balloon flight

The flight of EUSO-Balloon was carried out on the night of August 24/25, 2014. Unless otherwise noted, the time is given hereafter in UTC on August 25, 2014.

EUSO-Balloon was launched from the Timmins Stratospheric Balloon Base at the Timmins Victor M. Power Airport; Latitude (Lat.) $48°34'13''$ N, Longitude (Long.) $81°22'05''$ W and 296 m asl., at 00:54 (on August 24 at 20:54 EDT; UTC -4). Between 03:08 and 08:08, the EUSO-Balloon telescope was operated pointing towards the nadir. The position and attitude during the flight were monitored by the on-board GPS receivers. The attitude of the EUSO-Balloon telescope was adjusted and checked before launch. Thus, the GPS data allow the estimation of the ground position of the optical axis.

At 08:20, the EUSO-Balloon telescope was separated from the balloon and descended towards one of the 'driest' landing zones along the flight track. At 08:59, it splashed down in a small solitary lake (Lat. $48°39'10''$ N, Long. $82°41'14''$ W; 303 m asl.). Thanks to the protective design that shields all sensitive components in the event of a water landing [43], EUSO-Balloon was recovered undamaged and still fully operational.

In this work, we only use the data acquired in the Time interval of Interest (ToI) between 03:08 and 05:48. It was during a dark, moonless night, excluding periods of astronomical twilight. The instrument was operating in its nominal mode, allowing for uncertainties in the subsequent analysis to be minimized. After this time interval, various engineering tests were conducted with a variety of setups and operation modes, for which the analysis would have been more complex and uncertain.

Figure 1 displays the GPS ground track of the EUSO-Balloon optical axis by the solid curve. The bold curve denotes the track during the ToI. The launch and landing positions are marked in addition to the hourly positions. The dashed lines enclose the Region of Interest (RoI) for this work. The color scale represents the Visible band Digital Number (VDN) from the 2013 DMSP (Defense Meteorological Satellite Program) satellite data [57].

13

VDN scales to the fluxes in the $0.35-2$ μm band by 64 integer levels. We make use of the annual average data in cloud-free conditions given every $30''$ grid in geographic coordinates, i.e., at a resolution of ∼610 m on the east-west and ∼930 m on the north-south directions. The VDN is 0 in most of the RoI, while the rest is registered with a VDN of 4 or higher.

During the ToI, EUSO-Balloon traveled ∼80 km to the west. The average elevation, h_0, of the terrain along the track was 296 m asl. The ground track of the EUSO-Balloon telescope includes populated and industrial zones around Timmins, while most of the other areas were forests and small lakes. There are potentially intense artificial light sources around Kamiskotia Lake, the largest water body in the RoI, with a diameter of 2.5 km. The ground track also passed ∼3.4 km from Montcalm Mine in the western part of the RoI.

Figure 2 displays the altitude, H_0, of the EUSO-Balloon telescope as a function of the UTC time, t. EDT local time is shown on the top. The ToI and the dark night period are indicated by the arrows.

At the beginning of the ToI, the EUSO-Balloon telescope reached 36.4 km asl. Until 03:30, it continued ascending to the float altitude of about 38.2 km which was maintained within a ∼±0.2 km oscillation with a ∼5 min period. At this altitude, the atmospheric pressure is ∼4 hPa. To avoid coronal discharge at such a low pressure that could lead to a breakdown of the entire mission, we limited the high voltage applied on the MAPMTs to −950 V against the nominal operational voltage of −1100 V.

The EUSO-Balloon telescope was freely rotating around the optical axis. To describe such a rotation, we define the orientation, Φ_0, of the telescope by the eastward angle, measured from the true north to the x-axis of the PDM. Hereafter, azimuth with respect to the horizontal coordinates is defined in the same way.

Figure 3 displays the orientation Φ_0 of the EUSO-Balloon telescope as a function of the time t. North, east, south and west directions correspond to $0°, +90°, \pm180°$ and $−90°$, respectively. The ToI is indicated by the arrow.

During the ToI, the EUSO-Balloon telescope tended to rotate eastward and

14

made four rotations in total. It also exhibited a torsion pendulum motion with a typical period of $\sim$153 s, estimated by Fourier transform. In the earlier part of the ToI, the maximum amplitude of the torsion pendulum motion was $\pm 150°$. The angular velocity, $\dot{\Phi}_0$, was $7°$ s^{-1} at maximum. After having reached the float altitude, the torsion driven motions damped over time.

The pointing direction of the optical axis of the telescope also varied with a similar trend. The maximum off-axis angle from the nadir is estimated to be $\sim$1.8° [58]. Such variation of the attitude is taken into account in the ground track shown on Fig. 1 which is used as a reference for location during the analysis.

From the GPS data, the ground speed, v_0, of the EUSO-Balloon telescope ranged between 2 and 15 m s^{-1} with an average $\langle v_0 \rangle$ of 8 m s^{-1} ($\approx$ 31 km h^{-1}) during the ToI. The typical ground speed at the float altitude was $\sim 8-12$ m s^{-1} between 03:30 and 04:45. It then tended to slow down.

Chasing the ground track of the EUSO-Balloon telescope, we operated a helicopter at a flight altitude of $\sim$3 km from where we generated EAS-like events by using a UV laser [59]. LED and xenon flashers were also used to provide calibration sources. Between 03:21 and 05:48, $\sim 1.5 \times 10^5$ laser shots followed by the flasher events were generated in various horizontal directions from the helicopter. A small fraction of such events are included in the data used in this work.

3.3. The elementary data

During the ToI, the EUSO-Balloon telescope was operated to acquire a packet from every pixel by the DP signals at $\sim$19 Hz except for the time interval between 04:36 and 05:13 when the acquisition rate was at 20 Hz. In the intervals of $03:47-03:51$ and $05:13-05:16$, the telescope was operated in a different mode for the system checks [60]. Excluding these checks, $\sim$150 min ($=$ 2.5 hours) of the operation time was assigned for the purpose of this work.

The total number, M, of packets used in the analysis is $\sim 1.5 \times 10^5$. Let $n_{i,j}$ be the count readout on the i-th pixel at the j-th sample in the packet. The

average count rate $\langle n \rangle$ over a packet is given as follows:

$$\langle n_i \rangle = \frac{1}{128} \cdot \sum_{j=1}^{128} n_{i,j}, \tag{1}$$

where the pixel number is hereafter referenced by the subscript i. The $\langle n \rangle$ value represents the average for the interval of 320 μs ($= 128 \times 2.5$ μs) with the total gate time of 294 μs ($= 128 \times 2.3$ μs). The time resolution is $\sim$52 ms ($\approx 1/19$ [Hz]) given by trigger rates. This value in most cases represents the average noise level due to diffuse light.

Figure 4 displays examples of the $\langle n \rangle$ values of all the pixels on the PDM. Malfunctioning pixels are blackened out. Along with the GPS data, the left and right panels correspond to the packets acquired at (i) 03:09 and (ii) 05:47, respectively. The dimension of the PDM is shown in the right.

For further analysis, we use such 'snapshots' of the $\langle n \rangle$ values from Eq. (1) obtained every packet, along with the GPS data to form the elementary data set. These examples are chosen from the data obtained at the beginning and the end of the ToI. At the time of Example (i), EUSO-Balloon was flying above the eastern part of Timmins. Pixels with $\langle n \rangle$ values exceeding those of the adjacent pixels, hereafter referred to as 'hotspots', can be seen. As for Example (ii), EUSO-Balloon was above the forest at the west end of the RoI where no significant artificial light sources are expected.

4. Analysis

The main goal of the analysis is to obtain the temporal variation of the UV light measured by the EUSO-Balloon telescope and its image projected on geographic coordinates. In this section, we describe the analysis procedures using the elementary data, results of the post-flight calibration [54, 55, 58, 61] and relevant simulations.

4.1. Count rate determination

In this work, we use the average count rate $\langle n \rangle$ over a packet from Eq. (1). The readout count n shows non-linearity with respect to the number, n_{pe}, of

16

photoelectrons (pe) collected on the first dynode. This relation is expressed by the following theoretical formula [62]:

$$n \cong n_{\mathrm{pe}} \cdot \exp\left(-\frac{\tau_0}{\tau_{\mathrm{GTU}}} \cdot n_{\mathrm{pe}}\right), \qquad (2)$$

where $\tau_0 \sim 30$ ns corresponds to the double pulse resolution in photon counting by the readout electronics and was experimentally determined [63]. Substituting the $\langle n \rangle$ value given by Eq. (1) for the n value in this equation, we can solve for the n_{pe} value. The solution is double-valued in most cases. We choose the lower value of the solutions and call the 'count rate', N, in units of pe pixel^{-1} GTU^{-1}.

For $n{=}1$ and 10 counts pixel^{-1} GTU^{-1}, the corresponding N values are 1.01 and 11.7 pe pixel^{-1} GTU^{-1}, respectively. In the case of $n \gtrsim 28$ counts pixel^{-1} GTU^{-1}, no solution exists. Thus we force $\langle n \rangle$ values to have an upper limit of $\sim$28. This gives the bound of $N < 68$ pe pixel^{-1} GTU^{-1}. The fraction of such cases is $\sim 10^{-5}$ of the whole $\langle n \rangle$ data set.

As seen in Example (ii) of Fig. 4, there are relative differences among pixels mainly due to the different efficiencies. To correct such differences, we apply the result from the post-flight calibration of the PDM [54]. For all the pixels, 'pixel efficiencies', ε, in terms of the ratio of the collected n_{pe} to the number of photons incident on the pixel area through the BG3 filter, were determined at a wavelength, λ, of 378 nm. Using a calibrated NIST photodiode with 1.5% accuracy, a few pixels in each MAPMT were absolutely calibrated with an accuracy of better than 3% based on the technique developed in Ref. [64]. The rest of the pixels were then relatively calibrated.

For the detection efficiency, $\varepsilon_{\mathrm{det}}$, the product of the photocathode's quantum efficiency and the collection efficiency of the MAPMT, and transmittance, T_{BG3}, of the BG3 filters, the wavelength dependence of the ε efficiency is given as follows:

$$\varepsilon_i(\lambda) = \varepsilon_{\mathrm{det},i}(\lambda) \cdot T_{\mathrm{BG3},i}(\lambda). \qquad (3)$$

The T_{BG3} value also accounts for the geometrical effect whereby the filter acts as a light guide and thus tends to slightly increase pixel efficiencies at the outer part of each MAPMT.

17

To ensure a high quality data set, we eliminated the malfunctioning pixels that are mostly due to the limited voltage [55, 63]. We further select the best calibrated 650 pixels to limit the absolute uncertainty $\Delta\varepsilon < 5\%$, leading to relative uncertainty $\Delta\varepsilon/\varepsilon$ of 7% for the pixel efficiency at 378 nm. With a large number of packets used in the analysis, these selected pixels are statistically sufficient for an analysis of the topics of interest. It is worth mentioning that the pixel efficiencies remained constant at a level of $\pm11\%$ as of the ratios between the pre- and post-flight calibrations. The check was performed for 448 subset pixels [63].

For the selected 650 pixels, the average, $\langle\varepsilon\rangle$, of pixel efficiencies at 378 nm is used as a reference as follows:

$$\langle\varepsilon(378 \text{ [nm]})\rangle = 19.3\% \pm 0.1\%. \tag{4}$$

The Standard Deviation (SD) in the $\varepsilon(378 \text{ [nm]})$ values for these pixels is $\sim3\%$, i.e., $\sim16\%$ of the average $\langle\varepsilon\rangle$ value. The N value is converted to the 'normalized count rate', $\hat{N}$, as follows:

$$\hat{N}_i = \frac{\langle\varepsilon(378 \text{ [nm]})\rangle}{\varepsilon_i(378 \text{ [nm]})} \cdot N_i. \tag{5}$$

To reject temporarily unstable pixels, we define the 'active pixels' as those with a non-zero N value. Using the $\hat{N}$ values of all the active pixels in the packet acquired at the time, t_m, the average $\langle\hat{N}\rangle$ value is given as follows:

$$\langle\hat{N}\rangle_m = \frac{1}{(\text{Number of active pixels})} \cdot \sum_i \hat{N}_i, \quad \text{with } N_i \neq 0 \tag{6}$$

where the packet number is hereafter indicated by the subscript m. On average, $\sim90\%$ of the selected pixels were active during the ToI.

4.2. The optics response model to incident directions

The EUSO-Balloon optics is optimized for the UV photons emitted from EASs, essentially a dynamic confined spot of light with a small apparent lateral spread focused on a limited area on the PDM. In general, the displacement, d, of the focal spot from the center of the PDM increases with the incident off-axis

angle, ϑ, from the optical axis. In this work, we evaluate the relation of these two values by using simulations of the optical system. Applying the EUSO-Balloon configuration [65], we make use of the GEANT4 module [66, 67] implemented in the $\overline{\text{Off}\underline{\text{line}}}$ framework [68].

Figure 5 displays selected examples from ray trace simulations on the cross section of the EUSO-Balloon telescope. The key configuration of the optics is indicated. The case of $\vartheta = 4.5°$ and $\lambda = 365$ nm is shown here, resulting in a nominal focal point at a displacement $d \approx 66$ mm.

At the focus, photons from a point-like source form a Point Spread Function (PSF). Due to the λ dependence of the refractive index, chromatic aberration is also prominent in the PSF. A fraction of the affected photons create characteristic halos and additional structures in the PSF. Each lens can occasionally cause refraction to large angles and backward reflection of photons. The former introduces errors in imaging due to the photons reaching the PDM away from the nominal focal point. The latter reduces the photon collection efficiency.

Determination of the PSF and its centroid is not trivial, particularly outside of the $\sim 330\text{–}400$ nm band where SNR for focusing point-like light is designed to be maximum for EAS detections. In addition, at $\lambda \lesssim 330$ nm, absorption of photons in the PMMA lenses is significant [44, 45]. For this work, these effects must be taken into account only in the interpretation for the absolute intensity of diffuse light. A detailed discussion is given in Sec. 6.

When simulating photons from various ϑ angles on a fixed argument, φ, with respect to the PDM x-axis, those reaching the PDM form a high density band along the line at $\sim \varphi + 180°$. The photons incident from a given ϑ angle mostly contribute to the density around a particular displacement d on this line. The relation between these quantities is ideally approximated by a linear function as follows:

$$d \approx \left\langle \frac{\partial d}{\partial \vartheta} \right\rangle \cdot \vartheta, \quad \text{for } d \lesssim 82.5 \text{ mm.} \tag{7}$$

Based on this assumption, the derivative of the relation can be determined by

19

Table 1: Summary of the derivative $\langle \partial d / \partial \vartheta \rangle$ by fitting simulated results for different wavelengths λ and incident arguments φ' with respect to the nearest PDM axis.

	$\langle \partial d / \partial \vartheta \rangle$ [mm per 1°]		
	λ=330 nm	λ=365 nm	λ=400 nm
$\varphi' = \pm 0°$	14.20 ± 0.08	15.01 ± 0.03	14.73 ± 0.03
$\varphi' = \pm 15°$	14.29 ± 0.08	15.00 ± 0.03	14.70 ± 0.02
$\varphi' = \pm 30°$	14.29 ± 0.07	15.00 ± 0.02	14.72 ± 0.02
$\varphi' = \pm 45°$	14.33 ± 0.05	15.15 ± 0.02	14.80 ± 0.01

fitting simulated results. Due to the non-circular optics and optical distortion, azimuthal dependence also needs to be taken into account. The optical structure is symmetric with respect to both axes of the PDM. In this way, φ angles from both reference axes on the PDM are equivalent.

Table 1 summarizes the derivatives $\langle \partial d / \partial \vartheta \rangle$ in Eq. (7) in the matrix of the wavelengths λ and arguments φ' with respect to the nearest PDM axis. The second terms indicate the uncertainty in fitting.

In this work, we use a representative value of the derivative in Eq. (7) as follows:

$$\left\langle \frac{\partial d}{\partial \vartheta} \right\rangle \equiv 14.6 \text{ mm per } 1°. \tag{8}$$

We apply this equation to all parts of the PDM. Within the simulated combinations, this value has a maximum uncertainty of $\sim \pm 0.6$ mm per 1°, on the order of $\sim 4\%$ to Eq. (8).

According to Eqs. (7) and (8), we assign a nominal direction seen by each pixel at its center position (x, y) represented by ϑ and φ angles as follows:

$$\begin{pmatrix} x_i \\ y_i \end{pmatrix} \cong -\left\langle \frac{\partial d}{\partial \vartheta} \right\rangle \cdot \vartheta_i \cdot \begin{pmatrix} \cos \varphi_i \\ \sin \varphi_i \end{pmatrix}. \tag{9}$$

As seen in Fig. 5, the PSF may extend beyond the size of a pixel. A certain fraction of the photons on the pixel are not from the nominal FoV of that pixel. The inverse function of Eq. (9) can thus only deduce a likely incident direction of each photon reaching the PDM.

20

₆₁₃ The reciprocal of the derivative $\langle \partial d/\partial \vartheta \rangle$ is equivalent to 'plate
₆₁₄ scale.' The nominal angle of view, α_{pix}, seen by each pixel is
₆₁₅ $\approx 0.20°$ $(= 2.88 \,[\mathrm{mm}]/14.6\,[\mathrm{mm \ per \ 1°}])$. Along the PDM axis, considering
₆₁₆ ± 3 MAPMTs yields an equivalent dimension of ± 82.5 mm $(= \pm 3 \times 27.5\mathrm{mm})$ as
₆₁₇ seen in Fig. 4. By doubling the ϑ value in Eq. (7) to match $d = 82.5$ mm, the
₆₁₈ nominal angle of view, α_{PDM}, of the PDM is defined as follows:

$$\alpha_{\mathrm{PDM}} \approx 2 \cdot \left(\frac{82.5 \,[\mathrm{mm}]}{14.6\,[\mathrm{mm \ per \ 1°}]} \right) = 11.3°. \tag{10}$$

₆₁₉ As a reference, the corresponding length, L_{PDM}, projected on the level of
₆₂₀ $h_0 \ll H_0$ is given by:

$$L_{\mathrm{PDM}} \sim 2\,(H_0 - h_0) \cdot \tan\left(\frac{\alpha_{\mathrm{PDM}}}{2} \right) \approx 7.5\,[\mathrm{km}] \cdot \left(\frac{H_0}{38\,[\mathrm{km}]} \right). \tag{11}$$

₆₂₁ *4.3. Imaging the normalized count rates on geographic coordinates*

₆₂₂ To describe the incident direction of photons, we define a polar coordinate
₆₂₃ system by the nadir angle, Θ, and the azimuth, Φ, at the EUSO-Balloon
₆₂₄ telescope. We assume that the position of the telescope is above the GPS
₆₂₅ ground track of the optical axis, displayed in Fig 1.

To correlate assigned direction to the pixel, the corresponding incident
direction can be expressed as follows:

$$\vartheta \equiv \Theta \tag{12a}$$

$$\varphi \equiv \Phi - \Phi_0(t), \tag{12b}$$

₆₂₆ by taking into account the orientation Φ_0 of the telescope as shown in Fig. 3.

₆₂₇ Figure 6 illustrates the key geometry used in the analysis. Definitions of key
₆₂₈ points and coordinate systems are labeled.

To image the normalized count rates $\hat{N}$ plotted on geographic coordinates,
we assume that the count rate in each pixel is purely due to the photons
incident from the assigned nominal direction. In addition to those emitted
in this direction, photons may have been scattered, e.g. by clouds in the line
of sight. We map the distribution according to Point $\mathrm{G}(X, Y, h_0)$ independent

21

of local elevation. Assuming that the Earth is a globe with a radius $R_\oplus$, the distance, r, of Line Segment $\overline{\text{GE}}$ can be expressed using the cosine theorem as follows:

$$r = (R_\oplus + H_0) \cdot \cos\Theta$$
$$- \sqrt{(R_\oplus + h_0)^2 - (R_\oplus + H_0)^2 \cdot (1 - \cos^2\Theta)} \qquad (13a)$$
$$\approx \frac{H_0 - h_0}{\cos\Theta}. \qquad (13b)$$

Equation (13a) is important for similar analyses with data acquired by satellite-based missions with much wider FoV telescopes.

In this work, we use Eq. (13b) as the effect of the Earth's curvature is small for $L_{\text{PDM}} \ll R_\oplus$ or/and $H_0 \ll R_\oplus$. Point G (X, Y, Z) is given by:

$$\begin{pmatrix} X \\ Y \\ Z \end{pmatrix} = \begin{pmatrix} r \cdot \sin\Theta \sin\Phi \\ r \cdot \sin\Theta \cos\Phi \\ h_0 \end{pmatrix}. \qquad (14)$$

Using the GPS data of the ground position of the optical axis at Point O′, geographic coordinates in radians at Point G are located to as follows:

$$(\text{Lat.}) = \frac{Y}{R_\oplus + h_0} + (\text{Lat. at Point O}') \qquad (15a)$$

$$(\text{Long.}) = \frac{X}{(R_\oplus + h_0) \cdot \cos(\text{Lat.})} + (\text{Long. at Point O}'). \qquad (15b)$$

To analyze the geographic distribution of $\hat{N}$ values defined by Eq. (5), the RoI is treated as a grid with a separation of $1.8''$ in geographic coordinates which corresponds to ~ 37 m for the east-west X- and ~ 56 m for the north-south Y-directions. With a ~ 130 m $(= \alpha_{\text{pix}} \cdot H_0)$ square projected area per pixel, it may be shared by up to twelve grid points for $H_0 = 38$ km.

The $\hat{N}$ value of every active pixel and packet is filled to any grid point within the projected pixel area. As a function of the packet time t_m, the combinations of the i-th pixel and the k-th grid point are indicated as follows:

$$\delta_{i,k}(t_m) = \begin{cases} 1, & \text{overlapping} \\ 0, & \text{otherwise,} \end{cases} \qquad (16)$$

22

where the grid point number is hereafter denoted by the subscript k. Using all the available data, the average, $\langle \tilde{N} \rangle$, of the $\hat{N}$ values projected on the grid point is evaluated by using all involved packets as follows:

$$\left\langle \tilde{N} \right\rangle_k = \frac{\displaystyle\sum_m \sum_i \left[\delta_{i,k}(t_m) \cdot \hat{N}_i(t_m) \right]}{\displaystyle\sum_m \sum_i \delta_{i,k}(t_m)}. \tag{17}$$

The total number of grid points, K, is 3.8×10^5, where at least one packet is used to determine the $\langle \tilde{N} \rangle$ values. For the discussion in Sec. 6, we also make use of data with a coarser grid separation.

5. Results

5.1. The time evolution of the normalized count rates

In this section, we present two main results from the primary analyses described in Sec. 4. The first is the time evolution of the normalized count rates and the second is their distribution projected onto geographic coordinates. The statistical errors and uncertainties derived from additional factors are also estimated. Due to the selection criterion imposed on the pixels, the normalized count rates have a relative uncertainty of 7% in pixel efficiencies. The detailed discussion and interpretation are given in Sec. 6.

Figure 7 displays the average normalized count rates $\langle \hat{N} \rangle$ defined by Eq. (6) as a function of the packet time t_m. Data are partly eliminated due to a temporary hardware problem at 04:17 and due to a transient instability of the electronics around 04:58 and 05:07 resulting in high count rates in a few specific MAPMTs [26]. Interruptions starting at 03:47 and 05:13 were due to the system checks.

In the time interval between 04:38 and 04:52, referred to as Case (a), when the $\langle \hat{N} \rangle$ values are low and stable, the average $\langle N \rangle$ values are evaluated by several times 10^4 independent samples from the active pixels. In typical packets in Case (a), all or almost of all 650 selected pixels were active and the statistical error is irrelevant. The relative SD, $\hat{\sigma}/\langle \hat{N} \rangle$, among these pixels is on the order of

23

$\sim 15\%$. This deviation includes the non-uniform response of the optics to diffuse light and possible non-uniform light distribution in the FoV.

When this is not the case, and $\langle \hat{N} \rangle$ values are relatively high in particular during the early part of the ToI, their deviation among pixels is large due to the light source distribution inside the observation area as expected in Fig. 1. In this time interval, the number of active pixels frequently varies. The definition of normalized count rates by Eq. (2) may introduce a systematic uncertainty on the $\langle \hat{N} \rangle$ values due to the pile-up effect in response to high intensity light sources. Around 03:15, such a case is found. The $\langle \hat{N} \rangle$ value is suppressed in this case.

After 03:21, flasher and laser events were generated inside the observation area of the EUSO-Balloon telescope. Although no synchronization was made with the EUSO-Balloon telescope, signals from such events were observed and recognized in a few hundred packets by a specific analysis [26, 59]. These packets are included in the analyzed data. At the flight altitude of the helicopter, the corresponding length to the diagonal of the nominal FoV is ~ 10 km. Any laser event thus does not exceed ~ 32 μs, i.e., it takes at most 13 samples to cross this length at the speed of light. In this way, the impact on the displayed results is negligible.

5.2. The normalized count rates projected onto geographic coordinates

Figure 8 displays the average normalized count rates $\langle \tilde{N} \rangle$ on grid points defined by Eq. (17) projected onto geographic coordinates. The shaded area represents the area for which there are no determined $\langle \tilde{N} \rangle$ values.

The uncertainties in $\langle \tilde{N} \rangle$ value are correlated with that of location. Bad assignment of the nominal direction seen by each pixel introduces an artificial fluctuation into Eq. (17). In the following, the maximum uncertainty in location, in terms of misplacement from the position given by Eqs. (15a) and (15b), is estimated for the float altitude $H_0 = 38$ km. Unless otherwise mentioned, they are intended to represent the positions seen at the corners of the nominal FoV.

The statistical error of the $\langle \tilde{N} \rangle$ values primarily depends on the number,

24

$\sum_m \sum_i \delta_i(t_m)$, of measured packets per grid point. It can be up to 130 packets with an average of $\sim$12. In general, the grid points near the boundary area have a few packets used.

For the grid points where more than one packet is used, the *corrected sample standard deviation*, $\tilde{\sigma}$, can be calculated. With respect to the $\langle\tilde{N}\rangle$ values given by Eq. (17), the relative SDs, $\tilde{\sigma}/\langle\tilde{N}\rangle$, from 3.6×10^5 grid points are distributed with the mean value of $\sim$23%. For this grid resolution, the mean of the relative errors to the average $\langle\tilde{N}\rangle$ values is $\sim$13%.

At the typical ground speed $\langle v_0\rangle$, EUSO-Balloon traversed the L_{PDM} length corresponding to the nominal angle of view α_{PDM} for a duration of around 15 min ($\sim L_{\mathrm{PDM}}/\langle v_0\rangle$). The motion and rotation of the EUSO-Balloon telescope could lead to a difference in time between the first and last measured packets of up to $\sim$40 min. The local time of the ToI was $23{:}08 - 01{:}48$. Particularly in the populated zone, variability due to human activities cannot be ruled out.

The PSF intrinsically introduces errors in location. Due to the dependence on the wavelength and incident direction of photons, the relevant errors cannot be uniquely formulated. Deduced from a compact hotspot seen in Example (i) of Fig. 4, such errors are supposed to be relatively small, compared with those introduced by the analysis process. An additional discussion of these errors is given in Sec. 6.

Since we assume the α_{PDM} angle, using Eqs. (7) and (8), the maximum uncertainty of $\sim$4% from these equations is propagated to the uncertainty, $\Delta\vartheta$, in assigned pixel direction, which can be up to $\approx 0.4°$ ($= 4\% \cdot \alpha_{\mathrm{PDM}}/\sqrt{2}$). In this way, the location of the grid points has an associated uncertainty, $H_0 \cdot \Delta\vartheta$, of up to $\sim$160 m.

In the region where the $\langle\tilde{N}\rangle$ values are determined, the elevations of the terrain range between 205 m and 410 m according to Ref. [69]. Thus their deviations, Δh, from the reference $h_0 = 296$ m are smaller than 120 m. The uncertainty, $\Delta h \cdot \alpha_{\mathrm{PDM}}/\sqrt{2}$, in location is less than $\sim$20 m.

During the flight, the alignment of the MAPMTs on the PDM might differ

25

from what was designed by up to ∼1 mm in the form of gaps between neighboring BG3 filters. Such a misplacement could introduce an error in the assigned direction by the order of ∼0.07° (= 1 [mm] / 14.6 [mm per 1°]) resulting in a ∼50 m uncertainty in the projected position in the whole observation area.

Particularly in the beginning of the ToI, large torsion was loaded resulting in rapid rotation and oscillation of the EUSO-Balloon telescope. Such effects were mitigated in the western part of the RoI. Uncertainties in the location of the grid points by using Eqs. (12a) – (15b) effectively increase the apparent size of the point-like sources. This results in broadening hotspots, as seen in the eastern part of the RoI.

During the ToI, the orientation of the EUSO-Balloon telescope was monitored every 1 s. Thus the maximum uncertainty, $\Delta\Phi_0$, of the orientation is ∼7° from its maximum angular velocity. It was the case in the early part of the ToI and in the eastern part of the RoI. This leads to the maximum error, $\left(L_{\mathrm{PDM}}/\sqrt{2}\right) \cdot \Delta\Phi_0$, in location to be ∼650 m. This effect then decreases with the time as rotation and oscillation damped during the flight in the ToI.

6. Discussion

In this section, we discuss the results of the EUSO-Balloon data from three aspects; imaging capability by comparing correlations between the measured count rates and ground-based sources mainly to validate the analysis method in use, discussions on the role of count rates in exposure for UHECR observations and the absolute intensity of diffuse light. The outlook for the further pathfinder missions follows.

6.1. Correlation between the normalized count rate distribution and ground-based sources

In Fig. 8, several hotspots and extended light sources in the Timmins area and structures in the Montcalm Mine area are clearly visible. In order to compare with a light source distribution mainly in the visible band, we use

26

the DMSP data shown in Fig. 1. To identify the counterparts to the hotspots, we utilize public online map services [69, 70] and Landsat Imagery [71].

Figure 9 displays an extract of the Timmins area from Fig. 8 with VDN contours of the DMSP data, as in Fig. 1. The scales and resolutions have been modified. The following labels are given to the areas of the local VDN maxima with their values in superscripts: Hoyle Mine (H), Bell Creek Mine (B), north shore of Porcupine Lake (P), downtown of Timmins (T), airport (A) and shore of Kamiskotia Lake (K). The inset shows the Montcalm Mine area (M) in the western part of the RoI.

Even with the different spatial resolutions, generic patterns of the normalized count rates $\langle \tilde{N} \rangle$ as seen in the RoI are in good agreement with the distribution of the visible light fluxes in the DMSP data. Except for Area (K), the hotspots are found in the areas of the local VDN maxima. Multiple hotspots can be easily recognized in Areas (H), (P) and (M).

In order to find the correlation with the known light sources, we define the hotspots as spatially confined zones with high $\langle \tilde{N} \rangle$ values. To avoid the selection of hotspots that are purely due to fluctuations, a cut of 120 pe GTU^{-1} is set on the sum of the $\langle \tilde{N} \rangle$ values of 24 $(= 6 \times 4)$ grid points, i.e., an average value of $\langle \tilde{N} \rangle > 5$ pe pixel^{-1} GTU^{-1}. The grid separation in this discussion corresponds to a $\sim$220 m on both coordinates.

Table 2 summarizes the 16 selected hotspots. Key measured values, the ground-based counterpart sources and general remarks on the hotspots are described therein. The presented counterpart sources are found using Refs. [69, 70, 72].

For each hotspot, the maximum $\langle \tilde{N} \rangle$ grid point is likely to be correlated with its counterpart source. Hotspot (X1) is found in the area without a local VDN maximum. It coincides with the position of a mining ground at Pamour. In UHECR observations, good accuracy in location is an essential requirement for the analysis of EAS events. The capability of finding temporary intense sources or ones not shown on the map also helps eliminate the fraction of the observation area.

27

Table 2: Summary of the 16 selected hotspots. The labels are given according to the areas of the VDN maxima in Fig. 9, except for Hotspot (X1). Using Refs. [69, 70, 72], counterpart sources for the maximum $\langle \tilde{N} \rangle$ grid points are given along with general remarks on the hotspots.

| Label | Nearest time | Maximum $\langle \tilde{N} \rangle$ grid point | | $\langle \tilde{N} \rangle$ | Stretch | Counterparts to maximum $\langle \tilde{N} \rangle$ grid point |
		Lat.	long.			(Remarks for the whole hotspot)
(H1)	03:08	48°32′57″N	81°03′19″W	12	0.1	Industrial facility (boundary)
(H2)	03:08	48°32′54″N	81°04′22″W	23	1.4	Industrial complex with railroad yard, power plant etc.
(H3)	03:08	48°32′57″N	81°06′30″W	25	2.3	Mine pit (resolved into two pits ∼1 km apart)
(H4)	03:08	48°33′57″N	81°06′42″W	29	1.2	Mine pond
(X1)	03:09	48°30′55″N	81°06′48″W	11	0.2	Mine pit (no corresponding VDN maximum)
(B1)	03:16	48°33′10″N	81°10′47″W	62	2.2	Mining ground
(P1)	03:22	48°28′58″N	81°12′19″W	21	8.5	South Porcupine community (also resolved to Pottsville and Porcupine at ∼2–3 km to the east)
(P2)	03:30	48°28′13″N	81°14′02″W	31	0.5	Mining ground (boundary)
(P3)	03:31	48°27′59″N	81°14′52″W	23	0.2	Mine pit (boundary)
(T1)	03:34	48°29′39″N	81°16′54″W	6.3	0.3	Mining ground
(T2)	03:36	48°32′21″N	81°17′23″W	9.4	0.6	Cement factory
(T3)	03:37	48°28′33″N	81°19′15″W	29	27	Park on a residential zone boundary. Commercial facility and high $\langle \tilde{N} \rangle$ zones
(T4)	03:42	48°29′34″N	81°21′28″W	20	0.5	Industrial plant on the bank of Mattagami River
(A1)	03:46	48°33′55″N	81°22′13″W	16	0.1	Airport parking lot (boundary)
(M1)	05:30	48°40′00″N	82°05′45″W	11	0.4	Mining ground
(M2)	05:30	48°40′26″N	82°05′56″W	11	0.1	Facility ∼ 0.9 km from the counterpart of Hotspot (M1)

Nearest time indicates for the closest approach to the maximum $\langle \tilde{N} \rangle$ grid point and EUSO-Balloon.

$\langle \tilde{N} \rangle$ values are given in units of pe pixel^{-1} GTU^{-1}. The stretch of the confined hotspot area is indicated in units of km^2.

Hotspots (H1), (P2), (P3) and (A1) are measured near the boundary of the nominal FoV with a limited number of packets.

In the following, we discuss some of the characteristic hotspots and their counterparts. Additionally, lower $\langle \tilde{N} \rangle$ values are found in some areas which contain potential light sources. Possible interpretations for such cases are also given.

In Example (i) of Fig. 4, Hotspot (H1) is recognized in the bottom-right MAPMT. Hotspot (X1) is in the upper part of the PDM. In the same example, Hotspots (H2) and (H3) are clearly identified. Hotspot (H4) is on the bottom edge.

Hotspot (H1) illustrates a typical PSF for the photons from a compact source with a scale of 50–100 m. It spreads over $\sim 3 \times 3$ pixels, which corresponds to $\sim 0.6°$. The extent of the hotspots seen in Figs. 8 and 9 is broadened by uncertainties derived from the analysis. In the case of intense light sources, the breadth of such images is also affected by the photons that are scattered by molecules in the atmosphere. This effect was also observed and recognized in the events from the LED and xenon flashers on the helicopter.

Before $\sim 04{:}00$, several hotspots contribute to the large variations of the $\langle \hat{N} \rangle$ value seen in Fig. 7. Distinctly high values are found around $03{:}14 - 03{:}16$. Apart from this, contributions from the individual hotspots are not distinguished early in the ToI. This behavior can be explained by the passage of Hotspot (B1) in the nominal FoV for a short interval. This hotspot contains the data with saturated count rates. Thus the $\langle \tilde{N} \rangle$ values shown in Table 2 represent the lower limits.

Moving forward in time through the ToI, the $\langle \hat{N} \rangle$ values then gradually decrease as seen in Fig. 7. The gradient of the $\langle \tilde{N} \rangle$ values with the distance from Area (A) is seen in Fig. 8. Such behavior extends even beyond the boundary of the non-zero-VDN area, possibly due to the presence of clouds in the FoV. The pilot of the helicopter reported such conditions between 04:07 and 04:19 by looking up at the sky.

Hotspot (T3) is the largest of the listed hotspots, in terms of its extent. It extends in a populated zone and continues into the neighboring forestry zones. Inside this hotspot, there are a few potential counterpart sources to the grid points which have locally high $\langle \tilde{N} \rangle$ values.

In contrast, relatively low $\langle \tilde{N} \rangle$ values are observed over the populated zone around the VDN maximum of Area (T). A possible interpretation is an unstable behavior of the PDM that decreases the number of active pixels. Such situations tended to occur where a large number of photoelectrons were generated in a broad part of the PDM. As for the impact of this effect on UHECR observations, detections of EASs are primarily suppressed in such an area with too intense light and only determination of the affected area is relevant. In the upgraded

29

electronics, such a problem has been overcome and a dynamic range of photon counting has been extended to a few hundred photoelectrons [73].

In Fig. 9, no clear hotspot appears in the $\langle \tilde{N} \rangle$ distribution near Area (K) where there are potential artificial light sources on the shore and at a nearby mining ground [69]. A possible explanation is that the VDN values in this area are no higher than 7 which is barely above the sensitivity of the DMSP data in the RoI. Thus, the $\langle \hat{N} \rangle$ values measured in this area may not have significant increases, particularly under possible cloudy conditions. As also seen in Fig. 7, data acquisition was interrupted at 04:17 when EUSO-Balloon flew above this area and the data amount contributes less to the $\langle \tilde{N} \rangle$ distribution.

In Area (M) in Figs. 8 and 9, there are Hotspots (M1) and (M2). The corresponding peaks are observed around 05:30 in Fig. 7. The maximum $\langle \tilde{N} \rangle$ grid point of Hotspot (M2) is $\sim$150–250 m away from the counterpart [72], which shows the location uncertainty in this part of the RoI.

At $\sim$05:44, additional peaks are found in Fig. 7. At that time, the potential light sources in Area (M) were well out of the nominal FoV of the EUSO-Balloon telescope. An interpretation of these peaks is that the attitude of the instrument might be affected and instantaneously pointed to the direction of Hotspots (M1) and (M2). The GPS data show a significant impulsive acceleration, $\ddot{H}_0$, of >2 m s^{-2} in the vertical direction in comparison to its root mean square $\sqrt{\langle \ddot{H}_0^2 \rangle} \sim$0.5 m s^{-2} over the ToI.

6.2. Implications for space-based UHECR observations

In previous work reported in this Journal [22], the scientific performance of the JEM-EUSO instrument and its expected exposure to UHECR observations have been discussed. For the baseline design of JEM-EUSO, thresholds for the trigger algorithms are set by the average count rates, $\bar{N}$, from diffuse light. They are dynamically applied first on the pixel level and then on the higher level of the PDM segment either on MAPMTs or ECs [26, 27].

In the aforementioned work, it was assumed that the effect from the Moon is the main component of the temporal $\bar{N}$ variation in the orbit. The impact from

30

the local light component, especially artificial light, was separately evaluated by analyzing the distribution of visible light fluxes from the DMSP data. These distributions were used to evaluate two parameters: the observational duty cycle, η, and the fraction, f_{loc}, of the area with intense local light sources.

The η value was given as a ratio of the observation time, T_{obs}, to the whole mission lifetime, T_0. The T_{obs} time is defined as the time when the trigger algorithms are operational. For instance, time under daylight, twilight and large moonlight has been eliminated.

The f_{loc} value was given as an average ratio of the area with intense light sources to the whole area covered by the ISS orbit. It represents the expected fraction within the instantaneous observation area that is partly or totally lost due to such sources, including cities, lightning, aurorae etc.

The results of the EUSO-Balloon mission allow for similar studies, but with real data, i.e., the $\langle \hat{N} \rangle$ distribution from Eq. (6) and the $\langle \tilde{N} \rangle$ distribution from Eq. (17). The data from this work cover a $\sim$2.5 hour time interval and a $\sim$780 km^2 area and thus the given distributions represent the particular case of the EUSO-Balloon flight. This time and area are small compared with those potentially achieved by space-based missions, i.e., several years of mission lifetime and an order of 10^8 km^2 area on the Earth.

Figure 10 displays the temporal $\langle \hat{N} \rangle$ distribution in terms of the packets as shown in Fig. 7. The histogram denotes the fraction of packets relative to the total number of packets, $M = 1.5 \times 10^5$. The unity of the distribution is normalized to the $\sim$2.5 hours of the time assigned for this work. The dashed curve shows the cumulative fraction above the given $\langle \hat{N} \rangle$ value.

In a large fraction of the ToI, the distribution contains not only diffuse light but also the artificial light sources. The time intervals when the nominal FoV was free from the influence of the local light sources are limited. The peak value of the distribution coincides with the typical $\langle \hat{N} \rangle$ value in Case (a).

Although the trigger algorithms need to consider further effects such as different pixel efficiencies [26], the average normalized count rates are used for a first order discussion. In practice, the η value is determined by the permissible

31

limit, $\bar{N}_{\text{lim}}$, of the average count rate which allows the trigger algorithms to be operational and is expressed as follows:

$$\eta\left(<\bar{N}_{\text{lim}}\right) \equiv \frac{T_{\text{obs}}}{T_0} = \frac{1}{T_0} \cdot \int_0^{\bar{N}_{\text{lim}}} \frac{dT}{d\bar{N}} \, d\bar{N}. \tag{18}$$

where $dT/d\bar{N}$ denotes the temporal $\bar{N}$ distribution in the mission lifetime. The histogram shown in Fig. 10 gives such a distribution in the ToI of the EUSO-Balloon flight. The cumulative fraction shown in Fig. 10 represents Eq. (18). The time intervals when the data were eliminated in Fig. 7 are excluded. The time between triggers is included as the time that the instrument was operational. In the real space-based mission, the trigger rate is far smaller and the count rates are only monitored for trigger algorithms.

For space-based observations, the main scientific outputs will be the energy spectrum and arrival direction distribution of UHECRs. Both require determination of the exposure, A, for UHECR observations. This should be described as a function of the energy E_0 and should be projected onto the celestial sphere with the orbit taken into account.

Under moonless, clear atmosphere conditions in dark areas presumably without the effect of artificial light, a reference count rate, N_0, is defined as the average of the $\bar{N}$ values from diffuse light. For such conditions, a reference function of the instantaneous aperture, $\dot{A}_0$, for UHECR observations is obtained by simulating a large number of EASs and the instrument response. The instantaneous aperture, $\dot{A}$, for different conditions of the diffuse light empirically scales by the $\bar{N}$ value as follows [17, 22]:

$$\dot{A}(E_0; \bar{N}) = \dot{A}_0\left(\sqrt{\frac{N_0}{\bar{N}}} \cdot E_0\right) \tag{19}$$

in units of km^2 sr. Here, the effects of clouds and the local light component have been omitted.

The $\bar{N}$ value is variable as a function of the time, T, in the mission lifetime. By integrating Eq. (19), the exposure for UHECR observations is given as a

32

function of the energy as follows:

$$A(E_0) \equiv \int_0^{T_0} \dot{A}\left(E_0, \bar{N}(T)\right) dT \tag{20a}$$

$$= \int_0^{\bar{N}_{\mathrm{lim}}} \left[\dot{A}_0 \left(\sqrt{\frac{N_0}{\bar{N}}} \cdot E_0 \right) \cdot \left(\frac{dT}{d\bar{N}} \right) \right] d\bar{N}. \tag{20b}$$

in units of km^2 sr yr. Here $\dot{A} = 0$ for the time intervals when no UHECR observation is undertaken, including the case of $\bar{N} > \bar{N}_{\mathrm{lim}}$.

For UHECRs with $E_0 \gtrsim 10^{20}$ eV, the baseline design of JEM-EUSO has a nearly constant geometrical aperture [17, 22]. Taking into account the effects of the clouds and local light, the overall exposure at the highest energies can be expressed as:

$$A(\infty) \approx \dot{A}_0(\infty) \cdot \kappa_{\mathrm{C}} \cdot \eta \cdot (1 - f_{\mathrm{loc}}) \cdot T_0, \tag{21}$$

where κ_{C} is the cloud efficiency. This parameter describes the ratio of the aperture taking into account the presence of clouds to the one for clear atmosphere conditions [17, 22, 52].

Figure 11 displays the areal $\langle \tilde{N} \rangle$ distribution in terms of the grid points as shown in Fig. 8. The clear and filled parts of the histogram indicate the fractions of the grid points with respect to the total number $K = 3.8 \times 10^5$ of grid points in the eastern and western halves, respectively. They are split at Long. $81°35'49''2$W. The dashed curve shows the cumulative fraction above the given $\langle \tilde{N} \rangle$ value.

The f_{loc} value in Eq. (21) is relevant to the cumulative fraction shown in the figure. Most of the area in the western half accounts for relatively low $\langle \tilde{N} \rangle$ values, while the eastern half is dominated by high values from the extended hotspots. It is important to recall the low $\langle \tilde{N} \rangle$ values around Area (T) in Fig. 8. In space-based UHECR observations, the presence of such intense light sources is also foreseen. In this way, these contributions may be properly taken into account in the calculation of f_{loc} values.

33

6.3. The absolute intensity of diffuse light

It is primarily diffuse light that is relevant for space-based UHECR observations. Its count rate, $\hat{N}_0$, for clear atmosphere conditions is important for EAS analysis of the existing instrument. Although EUSO-Balloon was not expected to detect EAS events, the corresponding absolute intensity I_0 could provide another reference value.

6.3.1. The normalized count rates under clear atmosphere conditions

As the reflectivity of the clouds is higher, the time interval and area with lowest count rates are considered to represent a case with little influence from clouds, i.e., clear atmosphere. Such conditions were present in Case (a) between 04:38 and 04:52 as mentioned in Sec. 5. At 04:36, 04:48 and 04:55, the pilot reported clear sky conditions above the helicopter.

In addition, similar conditions were considered to be present between 05:30 and 05:48 referred to as Case (b). The pilot confirmed such conditions at 05:29, 05:35 and 05:46. EUSO-Balloon was flying through and away from Area (M) as seen in Example (ii) of Fig. 4. $\langle \hat{N} \rangle$ values are as low as in Case (a) seen in Fig. 7 if the contributions associated with Hotspots (M1) and (M2) are eliminated by strictly using 67 pixels in two MAPMTs out of the 650 selected pixels.

Figure 12 displays the $\langle \hat{N} \rangle$ distributions for Cases (a) and (b) shown as the solid and dashed histograms, respectively. Each histogram is normalized to the total number of packets in use: 2.3×10^4 for Case (a) and 1.5×10^4 for Case (b).

For the reference $\hat{N}_0$ value, we quote the mode of the distribution for Case (a) obtained as follows:

$$\hat{N}_0 \approx 0.65 \text{ pe pixel}^{-1} \text{ GTU}^{-1}. \tag{22}$$

The pixels used in Case (b) are a subset of those used in Case (a). The distribution for Case (b) is similar to that of Case (a) with a slightly broader fluctuation due to fewer pixels and packets in use.

6.3.2. The optics response to diffuse light

As seen in Fig. 5, some photons from a given incident direction are occasionally detected far from the nominal focal point. They are more pronounced in diffuse light. To describe such effects, we perform a large number of ray trace simulations using the $\overline{\text{Offline}}$ setup described in Sec. 4. Photons are isotropically incident on the optics by sampling over the area, S_{sim}, wider than the opening entrance. The maximum incident off-axis angle, ϑ_{lim}, is set by the geometry of the baffle.

For a photon with a wavelength λ and incident direction given by the ϑ and φ angles, let $\beta(\lambda, \vartheta, \varphi)$ be the probability of reaching the pixel. Using ray trace simulations, the average, $\bar{\beta}$, for a given λ over the incident directions is obtained as follows:

$$\bar{\beta}_i(\lambda) \equiv \frac{1}{\Omega_{\text{sim}}} \cdot \int_{\Omega} \beta_i(\lambda, \vartheta, \varphi) \, d\Omega = \frac{N_{\text{hit},i}(\lambda)}{N_{\text{sim}}(\lambda)}, \tag{23}$$

where $N_{\text{hit},i}$ is the number of photons reaching the i-th pixel among the simulated N_{sim} photons, $d\Omega = \sin \vartheta \, d\vartheta \, d\varphi$ is the solid angle element and Ω_{sim} is written as follows:

$$\Omega_{\text{sim}} = \int_{\Omega} \cos \vartheta \, d\Omega = \int_0^{2\pi} \int_0^{\vartheta_{\text{lim}}} (\cos \vartheta \cdot \sin \vartheta) \, d\vartheta \, d\varphi. \tag{24}$$

Taking into account the pixel efficiency $\varepsilon(\lambda)$ from Eq. (3), the 'pixel acceptance', $\tilde{a}$, to diffuse light can be expressed as a function of the wavelength as follows:

$$\tilde{a}_i(\lambda) \equiv \varepsilon_i(\lambda) \cdot \bar{\beta}_i(\lambda) \cdot S_{\text{sim}} \cdot \Omega_{\text{sim}}. \tag{25}$$

It has the dimensions of area multiplied by solid angle. These two qualities cannot be decoupled due to the intrinsic PSF, absorption and scattering effects of the Fresnel lenses.

Figure 13 displays the average pixel acceptance $\langle \tilde{a} \rangle$ over the selected 650 pixels to diffuse light as a function of the wavelength. The shaded interval indicates the SD component, $(\bar{\sigma}/\langle \bar{\beta} \rangle) \cdot \langle \tilde{a} \rangle$, over these pixels due to the non-uniform optics response where $\bar{\sigma}$ is the SD of $\bar{\beta}$ probabilities.

Table 3: Relative abundances dI_0/I_0 of photons in different wavelength bands and spectrum-weighted pixel acceptance $\breve{a}$ for the diffuse light models.

Model	Relative abundance $\dfrac{dI_0}{I_0}$ in wavelength λ [nm] band					Spectrum-weighted pixel acceptance $\breve{a}$ [m^2 sr]
	$300-340$	$340-380$	$380-420$	$420-460$	$460-500$	
Airglow	37%	39%	18%	5%	1%	0.95×10^{-6}
Starlight	15%	27%	24%	20%	15%	0.88×10^{-6}
Light bulb	0%	1%	12%	31%	57%	0.44×10^{-6}

The ray trace simulations of diffuse light demonstrate the non-uniform response of pixels, which cannot be simply formulated. Above 330 nm the optical system introduces an uncertainty $\bar{\sigma}/\langle\bar{\beta}\rangle$ of $\sim$11% to the average.

6.3.3. An interpretation for the absolute intensity estimation

Due to the λ dependence of the $\tilde{a}$ values, the model of the differential spectrum $dI_0/d\lambda$ of the diffuse light is needed to interpret the data. The I_0 value of diffuse light should follow the relation given by:

$$I_0 = \int_\lambda \frac{dI_0}{d\lambda}\, d\lambda. \tag{26}$$

In this work, the λ=300–500 nm band is chosen as a reference according to the sensitive range seen in Fig. 13.

Over this band, the spectrum-weighted pixel acceptance $\breve{a}$ is given as follows:

$$\breve{a} = \frac{1}{I_0} \cdot \int_\lambda \left[\ \langle\tilde{a}(\lambda)\rangle \cdot \frac{dI_0}{d\lambda} \ \right] d\lambda. \tag{27}$$

To determine this value, a model of the relative spectrum $(1/I_0) \cdot (dI_0/d\lambda)$ of the diffuse light needs to be applied. In order to find a potential range of $\breve{a}$ values, we assume three spectrum models. Models of airglow and starlight are for the natural light sources. The light bulb model is for artificial sources.

Table 3 summarizes the relative abundances, dI_0/I_0, in different λ bands for the airglow, starlight and light bulb models together with the corresponding $\breve{a}$ value in Eq. (27). A value of unity corresponds to the intensity in the 300–500 nm band, according to Eq. (26).

The airglow model is deduced from the data taken by the Ultraviolet Visual Echelle Spectrograph (UVES) [74, 75]. The starlight model is quoted from Ref. [33]. The light bulb model is from Ref .[80], intended for a lower bound of the $\breve{a}$ value.

For the natural light source models, photons are first sampled according to these models. Using the Monte Carlo method by the 'libRatran' code [76, 77], these photons are then traced from the top of the atmosphere and the back-scattering in the atmosphere is simulated to obtain their spectra on the telescope at 38 km asl.

The airglow emission has a continuum spectrum characterized by prominent lines in the $300-400$ nm band. Its back-scattered light also shows a dominant abundance for short λ. The back-scattered starlight has a continuum spectrum with its differential intensity rising with increasing λ. Another potential natural light source is zodiacal light which has a similar spectrum to the starlight model. Its contribution is considered to be very little at the local solar time of ~ 0 h in the ToI.

Under clear atmosphere conditions, Rayleigh scattering by molecules is the dominant process of radiation transfer [78]. For the light of extraterrestrial origin, relative abundances below ~ 320 nm are largely suppressed due to absorption by ozone molecules [79]. The response of the optics also renders contributions below ~ 300 nm negligible.

For a given $\breve{a}$ value, the expected count rate N in response to this diffuse light with a given intensity, I, is written as follows:

$$N = \breve{a} \cdot I \tag{28a}$$

$$= 0.23 \ \left[\text{pe pixel}^{-1} \ \text{GTU}^{-1}\right]$$
$$\cdot \left(\frac{\breve{a}}{10^{-6} \ [\text{m}^2 \ \text{sr}]}\right) \cdot \left(\frac{I}{100 \ [\text{photon m}^{-2} \ \text{sr}^{-1} \ \text{ns}^{-1}]}\right), \tag{28b}$$

for the $300-500$ nm band. By substituting the measured count rate $\hat{N}_0 \approx 0.65$ pe pixel^{-1} GTU^{-1} in Eq. (28a), the consistent I_0 value is deduced for each model.

Table 4: I_0 values deduced for different spectrum models.

	$300 - 500$ nm	$300 - 400$ nm
Model (this work)	Consistent I_0 [photon m^{-2} sr^{-1} ns^{-1}]	
Airglow	$\sim$320	$\sim$260
Starlight	$\sim$300	$\sim$170
Light bulb	$\sim$640	$\sim$30

Table 4 summarizes consistent I_0 values in the $300 - 500$ nm and $300 - 400$ nm bands deduced for different spectrum models. According to abundances below 400 nm in Table 3, the intensities in the $300 - 400$ nm band were estimated. They may be compared with former experiments [34, 35, 36].

In Case (a), the diffuse light seen by the EUSO-Balloon telescope is mostly from airglow and starlight components with an unknown mixture. Artificial light is highly unlikely to dominate the measured count rate in the forest. Thus, the values listed for artificial light would give conservative constraints. Note that airglow is a dynamic phenomenon. Its intensity varies in time and geographic position as well as by the influence of geomagnetic activity and atmospheric tides [81]. These variations could even exceed these model dependences.

A possible lower limit may be inferred with a virtual ideal instrument by assuming that all the photons incident on the optics aperture would focus on the nominal angle of view α_{pix} of a pixel. As the pixel efficiency $\langle \varepsilon \rangle$ is maximum at $\sim$378 nm, the maximum possible pixel acceptance for such an instrument is given by $\langle \varepsilon(378 \text{ [nm]}) \rangle \cdot S_{\mathrm{opt}} \cdot (\alpha_{\mathrm{pix}})^2$ and is 2.2×10^{-6} m^2 sr. Applying it to Eq. (28b) yields $\sim$130 photons m^{-2} sr^{-1} ns^{-1} to the reference count rate $\hat{N}_0$ in Eq. (22).

With the assumed optics response model, further uncertainty in the $\breve{a}$ values may be derived from the response of the EUSO-Balloon instrument. By taking into account the 7% uncertainty $\Delta\varepsilon/\varepsilon$ in pixel efficiencies from the PDM calibration and the pixel acceptance dependence of $\sim$11%, the overall uncertainty is $\sim$13% $\left(= \sqrt{(\Delta\varepsilon/\varepsilon)^2 + (\bar{\sigma}/\langle\bar{\beta}\rangle)^2} \right)$. Although not all

selected 650 pixels gave pre-flight calibration, the selection of pixels allows $\pm 11\%$ level uncertainty of a possible variation of the pixel efficiency during the flight. As mentioned in Sec. 5, the relative SD in normalized count rates among pixels is $\sim 15\%$ during the Case (a) time interval and thus it is consistent with the hypothesis of illumination of uniform diffuse light within the uncertainty of $\sim 18\% \left(= \sqrt{(13\%)^2 + (11\%)^2} \right)$.

6.4. Outlook

The experimental studies on UV light as background continue through further pathfinder missions. A flight of EUSO-SPB using NASA's Super-Pressure Balloon (SPB) [82] was made over the South Pacific between April 24 and May 7, 2017 UTC [83]. On-ground tests and preparations of Mini-EUSO [84] are in progress with a possibility to be operated in 2019. A ground-based pathfinder experiment EUSO-TA [85] has been operated at the site of the TA experiment in Utah, USA. It is capable of measuring the night sky background, including direct airglow emission.

EUSO-SPB introduced and flew with upgraded subsystems relative to EUSO-Balloon, which solved some of the issues seen in the instrument. PSF was also improved that allowed better imaging capability, while most of the time it flew above the pattern-less ocean. EUSO-SPB had an autonomous trigger for EAS events that had been proven by the UV lasers at the site of the TA experiment. The operation of EUSO-SPB was undertaken from NASA's Mid-Latitude Super Pressure Balloon Launch Site at Wanaka Airport, New Zealand. It was terminated due to a gas leakage of the balloon envelope. As much data as possible were downlinked before the instrument was abandoned ~ 200 nautical miles south-east of Easter Island.

Thanks to the trigger system, EUSO-SPB had the potential to detect a few EAS events if it had flown as long as a few months achieved in the former SPB flights. The observable energy range of the cosmic rays was lowered to a few times 10^{18} eV. The data analysis of EUSO-SPB, more oriented to EAS detections and estimation of the exposure to cosmic rays as discussed in Sec. 6.2

is underway.

Mini-EUSO is a 25 cm telescope with a refractive Fresnel optics mounted on the UV-transparent, nadir-facing window of the Russian module *Zvezda* on the ISS. With one PDM, it is designed to observe a 44° square FoV, corresponding to a square of side ∼300 km on the Earth's surface. Orbiting above the airglow layer, Mini-EUSO is capable of measuring the sum of direct and indirect components of diffuse light. The ISS orbit that ranges within latitudes of ±51.6° allows for the measurements at various positions over the Earth.

It is expected to provide interesting data on UV-luminous phenomena in the upper atmosphere [86]. For example, it will be possible to achieve more detailed information on airglow emissions, in particular, variation over time and position on the Earth, as well as the response to solar and geomagnetic activities. Measurements with large observation area will provide an opportunity to investigate different scale phenomena in airglow science such as the effect of the atmospheric gravity wave [87].

7. Conclusions

The EUSO-Balloon mission was designed, constructed and flown operating a ∼1 m^2 refractive Fresnel optics and a prototype PDM. Towards space-based UHECR observations, it was the first pathfinder mission in the JEM-EUSO program that took in-flight measurements in August 2014. After an 8 hour stratospheric flight, the instrument was safely recovered, allowing post-flight calibration in the laboratory.

In this work, we analyze ∼2.5 hours of the instrument data, in conjunction with the GPS data, post-flight PDM calibration and ray trace simulations. The main results obtained are the normalized count rates as a function of the time and their distribution on geographic coordinates over a ∼780 km^2 area. The high count rates with rapid variations are shown to be due to the developed area where such excesses are caused by the local artificial light sources. The lowest count rates are found when flying over forested areas. In general, the

40

image in the UV band is in good agreement with the distribution of the visible light fluxes measured by the DMSP satellites. By displaying the obtained image at higher resolution, more than a dozen hotspots are found and the corresponding counterpart light sources are clearly identified to ground facilities such as the airport, factories, and mines. In dark areas where EUSO-Balloon was operating under clear atmosphere conditions, ~ 310 photons $\mathrm{m}^{-2}\,\mathrm{sr}^{-1}\,\mathrm{ns}^{-1}$ in the $300-500$ nm band is deduced to explain the measured data by the simulations and assumed diffuse light spectra.

In this work, we demonstrate the imaging capability of the EUSO-Balloon telescope with wide-FoV large aperture refractive Fresnel optics. This gives new and complementary information compared with the former balloon-borne experiments that aimed at determining the absolute intensity of diffuse light. Possible impacts of diffuse light and local light to UHECR observations are discussed. The analysis methods developed can be applied to data to be obtained by the other pathfinders and real space-based missions, not only for the study of UV light as a background for UHECR observations but also to give insights on airglow science. These missions are capable of measuring and imaging a larger part of the night-Earth in the UV band.

41

References

[1] B.R. Dawson, M. Fukushima and P. Sokolsky, Prog. Theor. Exp. Phys., 12 (2017) 12A107.
https://doi.org/10.1093/ptep/ptx054

[2] F. Fenu et al., in Proc. of 35th Int. Cosmic Ray Conf. (Busan; 2017), Pos (ICRC2017) 486.
https://pos.sissa.it/301/486/pdf

[3] D. Ivanov, in Proc. of 34th Int. Cosmic Ray Conf. (The Hague; 2015), Pos (ICRC2015) 349.
https://pos.sissa.it/236/349/pdf

[4] D. Ivanov, in Proc. of 35th Int. Cosmic Ray Conf. (Busan; 2017), Pos (ICRC2017) 496.
https://pos.sissa.it/301/496/pdf

[5] I. Allekotte et al., Nucl. Instrum. Meth. A 586 (2007) 409.
https://doi.org/10.1016/j.nima.2007.12.016

[6] T. Abu-Zayyad et al., Nucl. Instrum. Meth. A 689 (2017) 87.

http://dx.doi.org/10.1016/j.nima.2012.05.079

[7] The Pierre Auger Collaboration, Science 357 (2017) 1266.

https://doi.org/10.1126/science.aan4338

[8] The Telescope Array Collaboration (R.U. Abbasi et al.), Astrophys. J. Lett.
790 (2014) L21.

http://doi.org/10.1088/2041-8205/790/2/L21

[9] R.U. Abbasi et al., Astrophys. J. 862 (2018) 92.

https://doi.org/10.3847/1538-4357/aac9c8

[10] J. Albraham et al., Nucl. Instrum. Meth. A 620 (2010) 227.

https://doi.org/10.1016/j.nima.2010.04.023

[11] H. Tokuno et al., Nucl. Instrum. Meth. A 676 (2012) 54.

https://doi.org/10.1016/j.nima.2012.02.044

[12] B. Keilhauer et al., EPJ Web Conf. 53 (2013) 01010.

https://doi.org/10.1051/epjconf/20135301010

[13] R. Benson and J. Linsley, in Proc. 17th Int. Cosmic Ray Conference, 8
(1981; Paris) 145.

http://adsabs.harvard.edu/abs/1981ICRC....8..145B

[14] R.E. Streitmatter et al. (the OWL Study Collaboration), AIP Conf. Proc.,
433 (1998) 95.

https://doi.org/10.1063/1.56149

[15] C.N. De Marzo (the Airwatch Collaboration), AIP Conference Proceedings,
433 (1998) 87.

https://doi.org/10.1063/1.56140

[16] O. Catalano et al., in P.A. Shaver, L. DiLella, A. Giménz
(eds.); "Astronomy, Cosmology and Fundamental Physics", ESO
ASTROPHYSICS SYMPOSIA (2003), 427.

[17] The JEM-EUSO Collaboration (J.H. Adams Jr. et al.), Exp. Astron. 40 (2015) 117.
https://doi.org/10.1007/s10686-014-9376-3

[18] The JEM-EUSO Collaboration (J.H. Adams Jr. et al.), Exp. Astron. 40 (2015) 153.
https://doi.org/10.1007/s10686-013-9371-0

[19] The JEM-EUSO Collaboration (J.H. Adams Jr. et al.), Exp. Astron. 40 (2015) 183.
https://doi.org/10.1007/s10686-014-9427-9

[20] P.A. Klimov et al., Space Sci. Rev. 212 (2017) 1687.
https://doi.org/10.1007/s11214-017-0403-3

[21] The JEM-EUSO Collaboration (J.H. Adams Jr. et al.), Exp. Astron. 40 (2015) 1 and the articles in the same issue 'Special Issue on the JEM-EUSO Mission'.
http://doi.org/10.1007/s10686-015-9483-9

[22] J.H. Adams Jr. et al., Astropart. Phys. 44 (2013) 76.
https://doi.org/10.1016/j.astropartphys.2013.01.008

[23] M. Casolino et al., in Proc. of 35th Int. Cosmic Ray Conf. (Busan; 2017), Pos (ICRC2017) 368.
https://pos.sissa.it/301/368/pdf

[24] P. Klimov et al., in Proc. of 35th Int. Cosmic Ray Conf. (Busan; 2017), Pos (ICRC2017) 412.
https://pos.sissa.it/301/412/pdf

[25] A. Olinto et al., in Proc. of 35th Int. Cosmic Ray Conf. (Busan; 2017), Pos (ICRC2017) 542.
https://pos.sissa.it/301/542/pdf

[26] G. Abdellaoui et al., Nucl. Instrum. Meth. A 866 (2017) 150.
https://doi.org/10.1016/j.nima.2017.05.043

[27] J. Bayer et al., in Proc. of 33rd Int. Cosmic Ray Conf. (Rio de Janeiro; 2013) ID0432. (preprint) In 'The JEM-EUSO Mission: Contributions to the ICRC2013', arXiv:1307.7071.

[28] E.g. World Data Center for Geomagnetism, Kyoto University; Geomagnetic Equatorial Dst index Home Page.
http://wdc.kugi.kyoto-u.ac.jp/dstdir/ (accessed on July 25, 2018).

[29] V.Y. Khomich, A.I. Semenov and N.N. Shefov; Airglow as an Indicator of Upper Atmospheric Structure and Dynamics, Springer-Verlag GmbH, Heidelberg (2008).
ISBN 978-3-540-75833.
http://www.springer.com/la/book/9783540758327

[30] G.G. Shepherd et al., J. Atmos. Sol.-Terr. Phys., 68 (2006) 2000.
http://doi.org/10.1016/j.jastp.2006.06.006

[31] A.V. Dmitriev et al., Planet. Space Sci. 59 (2011) 733.
http://doi.org/10.1016/j.pss.2011.02.010

[32] P. Bobik et al., in Proc. of 33rd Int. Cosmic Ray Conf. (Rio de Janeiro; 2013) ID0874. (preprint) In 'The JEM-EUSO Mission: Contributions to the ICRC2013', arXiv:1307.7071.

[33] C. Leinert et al., Astron. Astrophys. Suppl. Ser. 127 (1998) 1.
http://doi.org/10.1051/aas:1998105

[34] O. Catalano et al., Nucl. Instrum. Meth. A480 (2002) 547.
http://doi.org/10.1016/S0168-9002(01)00958-5

[35] S. Giarrusso et al., in Proc. of 28th Int. Cosmic Ray Conf. (Tsukuba) 2 (2003) 849.
http://www-rccn.icrr.u-tokyo.ac.jp/icrc2003/PROCEEDINGS/PDF/212.pdf

[36] L.M. Barbier et al., Astropart. Phys. 22 (2005) 439.
http://doi.org/10.1016/j.astropartphys.2004.10.002

[37] N. Sakaki, et al., in Proc. of 30th Int. Cosmic Ray Conf. (Merida), 5 (2007) 965.
http://indico.nucleares.unam.mx/event/4/session/39/contribution/497/material/paper/0.pdf

[38] P. Sokolsky, AIP Conference Proceedings, 433 (1998) 65.
https://doi.org/10.1063/1.56147

[39] R.M. Baltrusaitis et al., Nucl. Instrum. Meth., A240 (1985) 410.
https://doi.org/10.1016/0168-9002(85)90658-8

[40] G.K. Garipov et al., Astropart. Phys. 24 (2005) 400.
https://doi.org/10.1016/j.astropartphys.2005.09.001

[41] The JEM-EUSO Collaboration (J.H. Adams Jr. et al.), Exp. Astron. 40 (2015) 281.
http://doi.org/10.1007/s10686-015-9467-9

[42] P. von Ballmoos et al., in Proc. of 34th Int. Cosmic Ray Conf. (The Hague; 2015), Pos (ICRC2015) 322.
https://pos.sissa.it/236/322/pdf

[43] J. Evrard et al., in Proc. of 22nd ESA Symp. on European Rocket and Balloon Programmes (Tromso, Norway; 2015), 217.
ISBN 978-92-9221-294-0. ISSN 1609-042X., p.217

[44] JEM-EUSO Collaboration (Y. Takizawa and J.H. Adams), in Proc. of 30th Int. Cosmic Ray Conf. (Merida), 5 (2007) 1033.
http://indico.nucleares.unam.mx/event/4/session/39/contribution/823/material/paper/0.pdf

[45] Y. Takizawa et al., in Proc. of 31st Int. Cosmic Ray Conf. (Lodz; 2009), ID792.
http://icrc2009.uni.lodz.pl/proc/pdf/icrc0792.pdf

[46] K. Maekawa et al., in Proc. of 31st Int. Cosmic Ray Conf. (Lodz; 2009), ID103.

http://icrc2009.uni.lodz.pl/proc/pdf/icrc0103.pdf

[47] The JEM-EUSO Collaboration (J.H. Adams Jr. et al.), Exp. Astron. 40 (2015) 19.

http://doi.org/10.1007/s10686-014-9418-x

[48] Hamamatsu Photonics K.K.; 'PHOTOMULTIPLIER TUBES AND PHOTOMULTIPLIER TUBE ASSEMBLIES R11265U SERIES / H11934 SERIES'

https://www.hamamatsu.com/resources/pdf/etd/R11265U_H11934_TPMH1336E.pdf

(accessed on July 31, 2017).

[49] The JEM-EUSO Collaboration (J.H. Adams Jr. et al.), Exp. Astron. 40 (2015) 91.

https://doi.org/10.1007/s10686-015-9453-2

[50] Schott AG; 'BG3 filter data sheet (Status December 12, 2014)'.

https://www.schott.com/d/advanced_optics/71957ac1-e196-4963-b006-b2ad1830bf2f/1.5/schott-bandpass-bg3-jun-2017-en.pdf

(accessed on July 25, 2018).

[51] M. Unger, B.R. Dawson, R. Engel, F. Schussler and R. Ulrich, Nucl. Instrum. Meth. A588 (2008) 433.

https://doi.org/10.1016/j.nima.2008.01.100

[52] The JEM-EUSO Collaboration (J.H. Adams Jr. et al.), Exp. Astron. 40 (2015) 135.

http://doi.org/10.1007/s10686-014-9377-2

[53] V. Scotti and G. Osteria, J. Inst. 9 (2014) C03034.

https://doi.org/10.1088/1748-0221/9/03/C03034

[54] C. Moretto et al., in Proc. of 34th Int. Cosmic Ray Conf. (The Hague; 2015), Pos (ICRC2015) 655.

https://pos.sissa.it/236/655/pdf

[55] S. Dagoret-Campagne et al., in Proc. of 34th Int. Cosmic Ray Conf. (The Hague; 2015) Pos (ICRC2015) 607.

https://pos.sissa.it/236/607/pdf

[56] The JEM-EUSO Collaboration (Y. Kawasaki), in Proc. of 30th Int. Cosmic Ray Conf. (Merida), 7 (2007) 1037.

http://indico.nucleares.unam.mx/event/4/session/39/contribution/824/material/paper/0.pdf

[57] NOAA National Center for Environmental Information; 'Defense Meteorological Satellite Program (DMSP) data'.

https://ngdc.noaa.gov/eog/dmsp.html (accessed on March 14, 2015).

[58] C. Catalano; *Premières lumières du télescope EUSO-Ballon Vers la détection des rayons cosmiques ultra-énergétiques depuis l'espace* (in French; First light of the EUSO-Balloon telescope: toward the detection of ultra-high energy cosmic rays from space); PhD Dissertation, *l'Université Toulouse 3 Paul Sabatier*, France (2015).

https://tel.archives-ouvertes.fr/tel-01417298

[59] G. Abedellaoui et al., J. Inst., 13 (2018) P05023.

http://stacks.iop.org/1748-0221/13/i=05/a=P05023

[60] G. Osteria et al., in Proc. of 34th Int. Cosmic Ray Conf. (The Hague; 2015) Pos (ICRC2015) 659.

https://pos.sissa.it/236/659/pdf

[61] C. Catalano et al., in Proc. of 34th Int. Cosmic Ray Conf. (The Hague; 2015) Pos (ICRC2015) 622.

https://pos.sissa.it/236/622/pdf

[62] S. Pomme, Appl. Radiat. Isot. 66 (2008) 941.

https://doi.org/10.1016/j.apradiso.2008.02.038

[63] C. Moretto; *Étude du fonctionnement d'un télescope de lumière de fluorescence dans le cadre du projet EUSO-Balloon* (in French; Study of

48

a fluorescence telescope for the EUSO-Balloon project); PhD Dissertation, *l'Université Paris-Sud*, France (2016).

https://tel.archives-ouvertes.fr/tel-01239883

[64] C. Blasksley and P. Gorodezky, Nucl. Instrum. Meth. A 764 (2014) 198.

http://doi.org/10.1016/j.nima.2014.07.033

[65] B. Panico et al., in Proc. of 34th Int. Cosmic Ray Conf. (The Hague; 2015) Pos (ICRC2015) 667.

https://pos.sissa.it/236/667/pdf

[66] S. Agostinelli et al., Nucl. Instrum. Meth. A506 (2003) 250.

http://doi.org/10.1016/S0168-9002(03)01368-8

[67] Geant4 Collaboration; 'GEANT4: A toolkit for simulation of the passage of particles through matter'.

http://www.geant4.org/geant4/ (accessed on October 20, 2016).

[68] S. Argirò et al., Nucl. Instrum. Meth. A580 (2007) 1485.

http://doi.org/10.1016/j.nima.2007.07.010

[69] Natural Resources Canada; 'online mapping tool for National Topographic System'.

http://atlas.gc.ca/toporama/en/ (January 6, 2017)

[70] E.g. Google Maps; 'an online map service (satellite images for the region of interest are provided by DigitalGlobe).

https://www.google.ca/maps/place/Timmins,+ON/ (accessed on October 20, 2016).

[71] Earth Science Data Interface, University of Maryland; 'Landsat imagery covering Timmins region taken on August 26, 2009'.

ftp://ftp.glcf.umd.edu/glcf/Landsat/WRS2/p021/r026/L5021026_02620090826.TM-GLS2010/ (accessed on July 18, 2016).

[72] Bing Maps: 'Aerial image of Area (M)' dated April 2016'.
https://www.bing.com/maps?osid=d1f6cbb9-c3d4-4732-8b5a-eec702aeb741&cp=48.67,-82.1&lvl=16&style=h
(accessed on May 21, 2017).

[73] S. Bilin et al., "SPACIROC3: 100 MHz photon counting ASIC for
EUSO-SPB", Nucl. Instrum. Meth. A (in press)
https://doi.org/10.1016/j.nima.2017.12.060

[74] H. Dekker et al., in Proc. SPIE, Optical and IR Telescope Instrumentation
and Detectors, 4008 (2000) 534.
http://doi.org/10.1117/12.395512

[75] European Southern Observatory; 'UVES–Ultraviolet and Visual Echelle
Spectrograph'.
http://www.eso.org/sci/facilities/paranal/instruments/uves.html
(accessed on August 15, 2016).

[76] C. Emde et al., Geosci. Model Dev. 9 (2016) 1647.
http://doi.org/doi:10.5194/gmd-9-1647-2016

[77] B. Mayers et al.; 'libRatran website'.
http://www.libradtran.org/doku.php (accessed on September 1, 2016).

[78] A. Bucholtz, Appl. Opt. 34 (1995) 2765.
http://doi.org/doi:10.1364/AO.34.002765

[79] J.H. Seinfeld and S.N. Pandis; Atmospheric Chemistry and Physics: From
Atmospheric Chemistry and Physics: From Air Pollution to Climate
Change, 2nd Edition; John Wiley & Suns, Inc., Hoboken (2006).
ISBN: 978-0-471-72018-8.

[80] M. Conner; 'Light spectrum/spectrometer charts and raw data for common
lights'.
http://www.designingwithleds.com/light-spectrum-charts-data/ (accessed
on October 3, 2017).

[81] R.F. Pfaff Jr., Space Sci. Rev. 168 (2012) 23.
http://doi.org/10.1007/s11214-012-9872-6

[82] NASA Balloon Program Office; 'NASA Code 820 (Super Pressure Balloon)'.
http://sites.wff.nasa.gov/code820/spb.html (accessed on July 25, 2018).

[83] L. Wiencke et al., in Proc. of 35th Int. Cosmic Ray Conf. (Busan; 2017) Pos (ICRC2017) 1097.
https://pos.sissa.it/301/1097/pdf

[84] F. Capel et al., "A high resolution detector for the study of terrestrial and cosmic UV emission from the International Space Station", Adv. Space Res. (2017; in press).
https://doi.org/10.1016/j.asr.2017.08.030

[85] The JEM-EUSO Collaboration (J.H. Adams Jr. et al.), Exp. Astron. 40 (2015) 301.
http://doi.org/10.1007/s10686-015-9441-6

[86] R.R. Meier, Space Sci. Rev. 58 (1991) 1.
http://doi.org/10.1007/BF01206000

[87] S. Perwitasari, J. Geophys. Res. 120 (2015) 9706.
http://doi.org/10.1002/2015JA021424

51
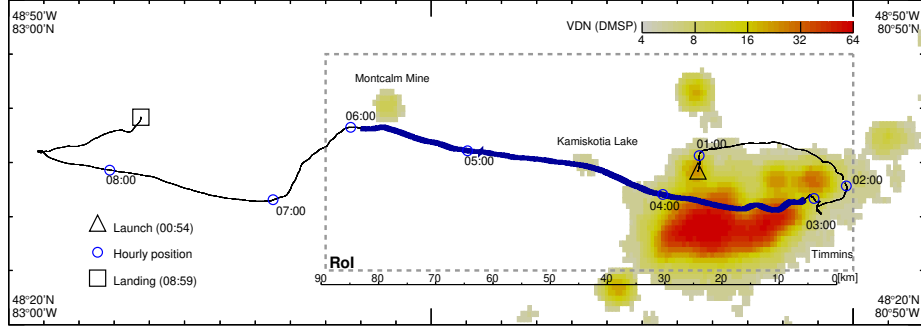
Figure 1: GPS ground track of the EUSO-Balloon optical axis shown by the solid curve. The VDN distribution is shown in color scale. A triangle and a square mark the launch and landing positions, respectively. The hourly positions are also marked by circles. The bold curve indicates the track during the ToI. The RoI is enclosed by the dashed lines.
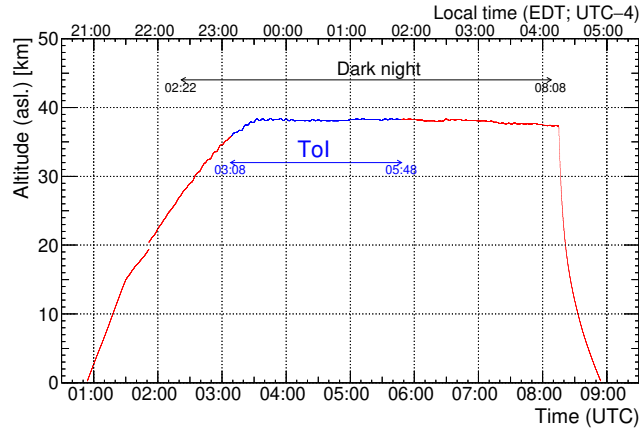
Figure 2: Altitude H_0 of the EUSO-Balloon telescope above sea level as a function of the UTC time t. The local EDT time is shown on the top. The upper and lower arrows indicate the dark night period and the ToI, respectively.

52
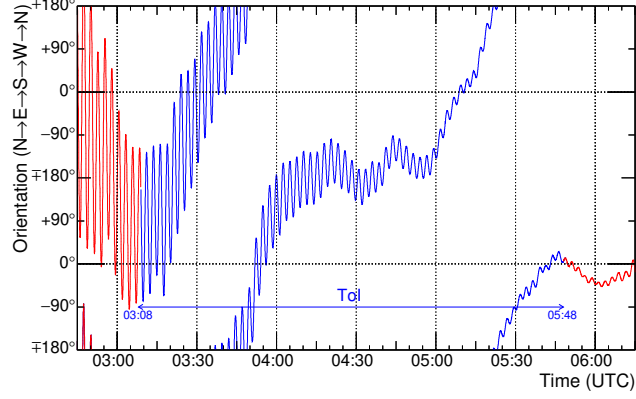
Figure 3: Orientation Φ_0 of the EUSO-Balloon telescope as a function of the time t. The arrow represents the ToI.
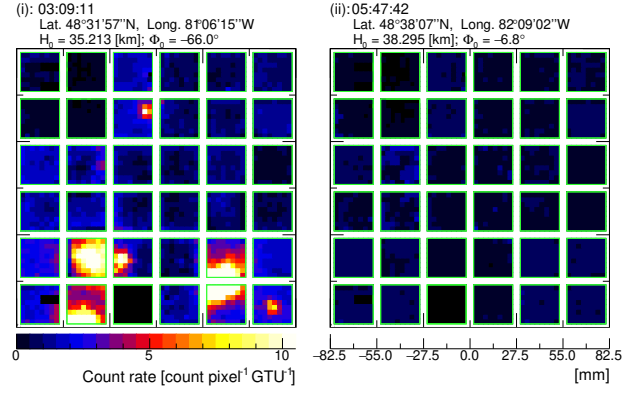
Figure 4: Examples of $\langle n \rangle$ values of all the pixels on the PDM for the packets acquired at (i) 03:09:11 and (ii) 05:47:42 on the left and right panels, respectively. Malfunctioning pixels are blackened out. The ground position of the EUSO-Balloon optical axis and the orientation of the telescope at these times are given on the top. Seen from the optics side, images are mirrored. The dimension of the PDM is shown in the right panel.
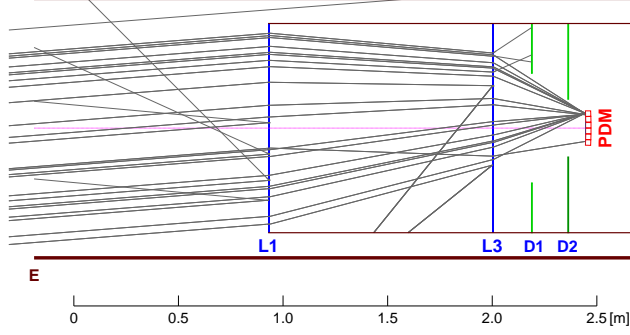
Figure 5: Selected examples of ray trace simulations for a point-like source at the incident off-axis direction $\vartheta = 4.5°$. The configuration of the front (L1) and rear (L3) lenses, opening entrance (E), diaphragms (D1) and (D2) and the PDM is shown on the cross section of the EUSO-Balloon telescope. In these examples for $\lambda = 365$ nm, the displacement $d \approx 66$ mm from the PDM center is a nominal focal point.
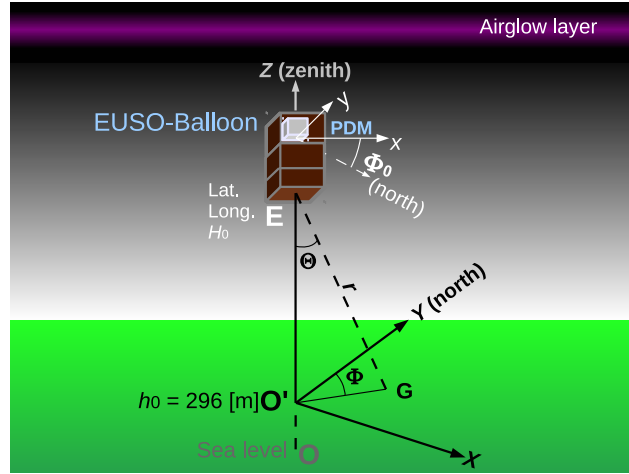
Figure 6: Geometry used in the analysis. The position of the EUSO-Balloon telescope is at Point E $(0, 0, H_0)$. In the direction of the nadir angle Θ and azimuth Φ, Point G (X, Y, h_0) is defined at the distance r from Point E. Point O$'$ indicates the position of the optical axis on $h_0 = 296$ m asl. The orientation Φ_0 of the telescope is defined as illustrated.
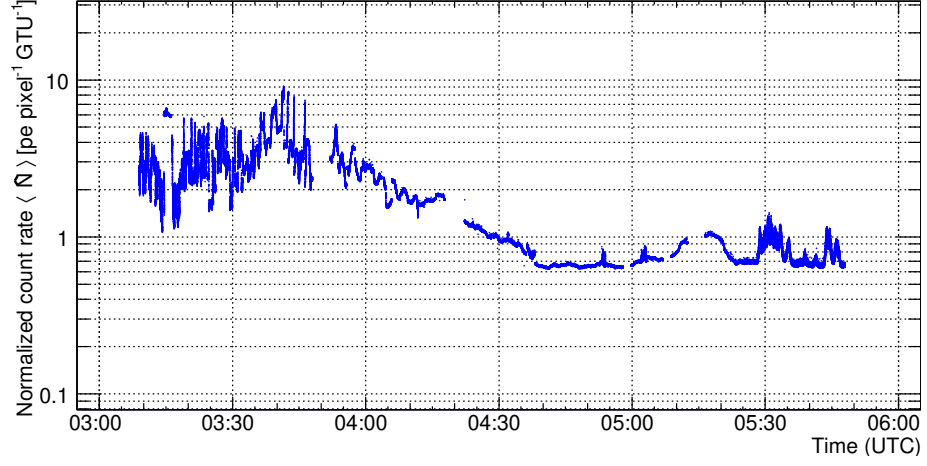
Figure 7: Average normalized count rates $\langle \hat{N} \rangle$ as a function of the packet time t_m. Data are partly eliminated due to a temporary hardware problem around 04:17 and due to a transient instability of the electronics around 04:58 and 05:07. Interruptions starting at 03:47 and 05:13 were due to a different operation mode for the system checks.
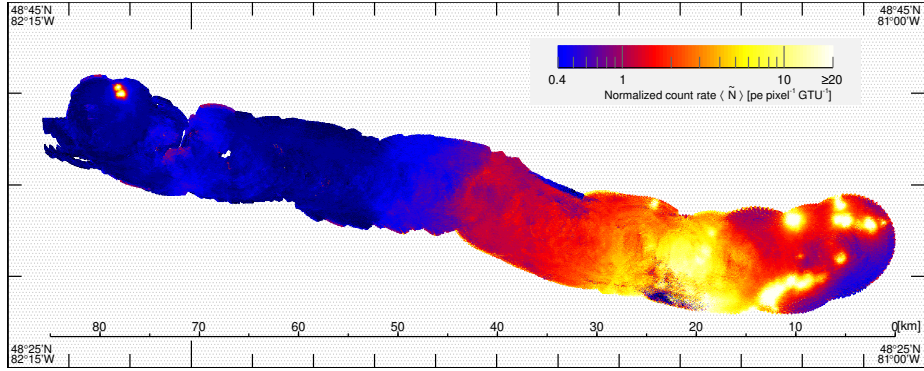

Figure 8: Normalized count rates $\langle \tilde{N} \rangle$ projected onto geographic coordinates. The shaded areas represent the area for which there is no determined $\langle \tilde{N} \rangle$ values. Coordinates on the corners are labeled together with ticks every $5'$ on both axes.
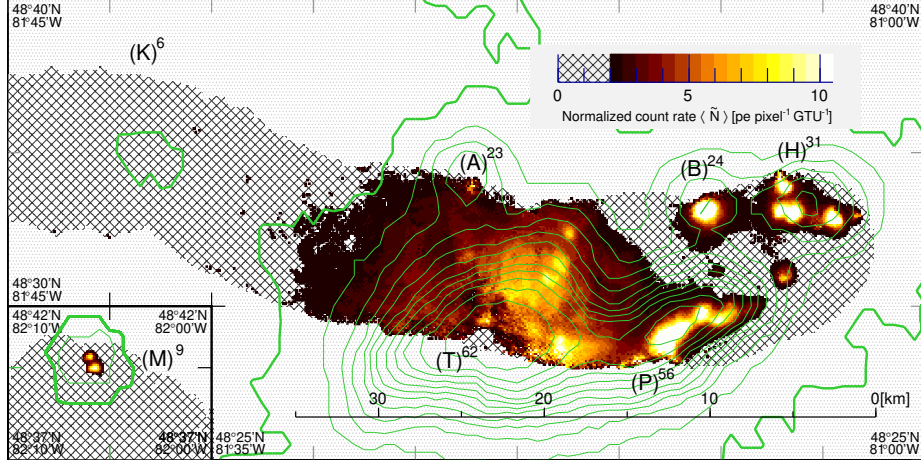
Figure 9: Extract from Fig. 8 shown with VDN contours overlaid, as in Fig. 1. The scales and resolutions have been modified. The hashed areas indicate the grid points with $\langle \tilde{N} \rangle <$ 1.5 pe pixel^{-1} GTU^{-1}. Bold contours are for VDN = 4 and thin ones are given at a step of 5. The local VDN maxima are labeled with their values in superscripts: Holye Mine (H), Bell Creek Mine (B), north shore of Porcupine Lake (P), Timmins downtown (T), airport (A) and shore of Kamiskotia Lake (K). The inset shows the Montcalm Mine (M) area in the western part of the RoI.
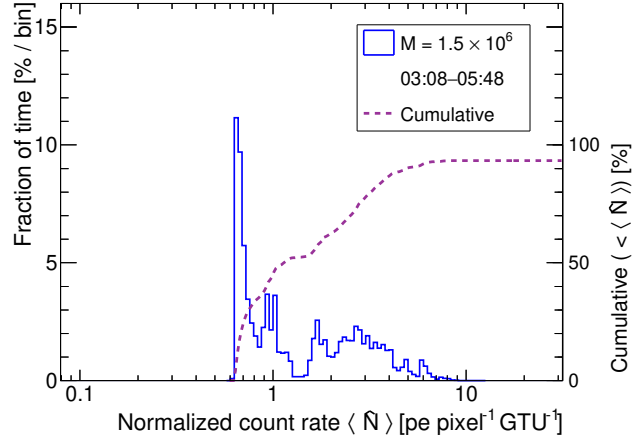

Figure 10: Temporal $\langle \hat{N} \rangle$ distribution in terms of the packets with respect to the total $M = 1.5 \times 10^5$. The unity of the distribution is normalized to the $\sim$2.5 hour time assigned for this work. The cumulative fraction below the given $\langle \hat{N} \rangle$ value is shown by the dashed curve to the scale on the right.
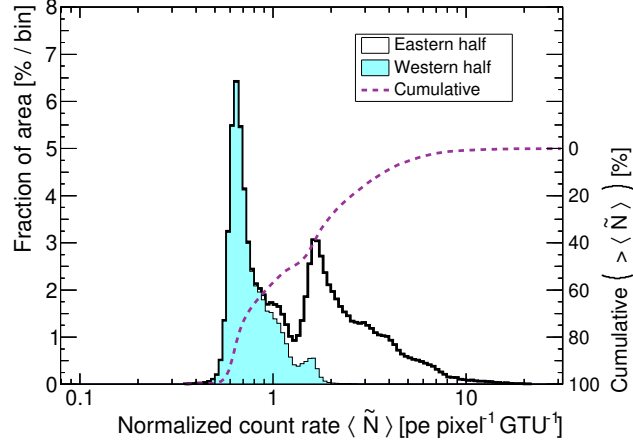
Figure 11: Areal $\langle \tilde{N} \rangle$ distribution in terms of the grid points with respect to the total $K = 3.8 \times 10^5$. The contributions from eastern and western halves whose areas are even are displayed by the clear and filled parts of the histogram, respectively. The cumulative fraction above the given $\langle \tilde{N} \rangle$ value is given by the dashed curve to the scale on the right.
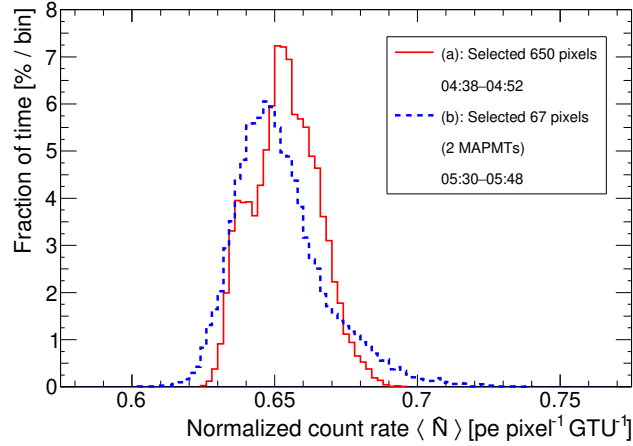

Figure 12: $\langle \hat{N} \rangle$ distributions for Case (a) of the active pixels between 04:38 and 04:52 and Case (b) of those from more strictly selected 67 pixels between 05:30 and 05:48 shown as the solid and dashed histograms, respectively. Each histogram is normalized to the total number of packets in use: 2.3×10^4 for Case (a) and 1.5×10^4 for Case (b).

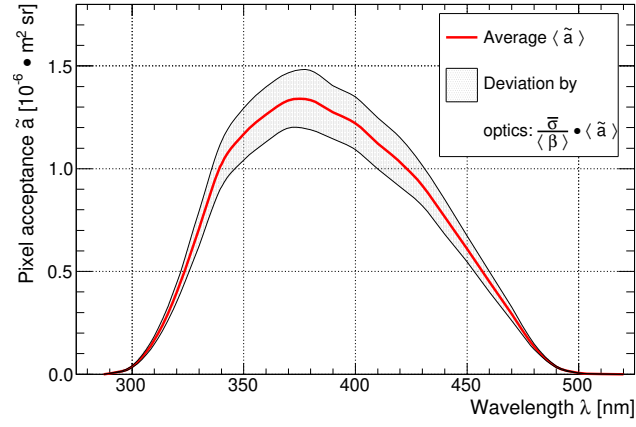Figure 13: Average pixel acceptance $\langle \tilde{a} \rangle$ over the selected 650 pixels to diffuse light as a function of the wavelength λ. The shaded interval indicates the SD component, $(\bar{\sigma}/\langle \bar{\beta} \rangle) \cdot \langle \tilde{a} \rangle$ over these pixels due to the non-uniform optics response.